Cenozoic lateritic weathering and erosion history of Peninsular India from 40 Ar/ 39 Ar dating of supergene K-Mn oxides

Nicolas J Bonnet, Anicet Beauvais, Nicolas Olivier Arnaud, Dominique Chardon, Mudlappa J Jayananda

Cenozoic lateritic weathering and erosion history of Peninsular India from $^{40}Ar/^{39}Ar$ dating of supergene K-Mn oxides

Nicolas J. Bonnet [1*], Anicet Beauvais [1*], Nicolas Arnaud [2], Dominique Chardon [3,4,5], Mudlappa Jayananda [6]

[1] Aix-Marseille Université (AMU), IRD (Institut de Recherche pour le Développement), CNRS (Centre National de la Recherche Scientifique), CEREGE (Centre Européen de Recherche et d'Enseignement des Géosciences de l'Environnement) UM34, BP 80, 13545 Aix-en-Provence, Cedex 4, France

[2] Université de Montpellier 2, Géosciences Montpellier, UMR CNRS 5243, 34095 Montpellier, France

[3] IRD, UMR 234, GET, 14 Avenue Edouard Belin, 31400 Toulouse, France

[4] Université de Toulouse, UPS (Université Paul Sabatier) OMP (Observatoire Midi-Pyrénées), 31400 Toulouse, France

[5] CNRS, GET, 31400 Toulouse, France

[6] Centre for Earth and Space Sciences, University of Hyderabad, P.O Central University Gachibowli, Hyderabad 500 046, India

Submitted to Chemical Geology, October 7th 2015

Revised, April 15, 2016

Accepted April 20, 2016

*Correspondings authors: nicolas.bonnet.geo@gmail.com; beauvais@cerege.fr

Abstract

Since Deccan Traps extrusion ~ 65 Ma ago, thick weathering mantles have developed over Peninsular India on both the western coastal lowland and adjacent plateau separated by the Western Ghats Escarpment. Manganiferous lateritic profiles formed by supergene weathering of Late Archean manganiferous protores are exposed on paleolandsurface remnants on both sides of the escarpment. Petrological and geochemical characterizations of samples from those Mn lateritic profiles allowed identifying cryptomelane (K-Mn oxide) dated by $^{40}Ar/^{39}Ar$ geochronology. The ages obtained document major weathering periods, ca. 53-50 Ma, and ca. 37-23 Ma in the highland, and ca. 47-45 Ma, ca. 24-19 Ma and discrete weathering pulses at ~ 9 Ma and ~ 2.5 Ma in the lowland. Old ages of the highland (53-50 Ma) and the lowland (47-45 Ma) indicate synchronous lateritic weathering across the escarpment at a time the peninsula started to drift across the equatorial belt. Intense weathering periods at ca. 53-45 and ca. 37-23 Ma are interpreted to reflect the Early Eocene climatic optimum and the onset of Asian monsoon regimes, respectively. The ages further indicate that most of the dissection of the highland must have taken place after ~ 23 Ma, whereas the lowland was weakly incised essentially after ~ 19 Ma. Our results also document divergent erosion and weathering histories of the lowland and the highland after the Eocene, suggesting installation of a dual climatic regime across the Western Ghats escarpment.

Keywords: $^{40}Ar/^{39}Ar$ geochronology; Supergene Mn-oxides; Mn-ore deposits; Lateritic weathering; Cenozoic; India

1. Introduction

Chemical rock weathering that results in the accumulation of metals such as Al, Fe or Mn, and relative depletion of silica and base elements, produce lateritic regoliths covering shields in the tropical belt. Weathering processes are intense under wet and warm climate that characterizes most tropical forest's soil environments (Pedro, 1968; Ollier, 1988; Nahon, 1991; Tardy, 1997). Metals are mostly retained in duricrusts capping thick weathering profiles, which are, in turn, partly preserved from mechanical erosion. Therefore, old lateritic weathering profiles several tens of meters thick may be preserved on paleolandsurface remnants for several millions years (Bárdossy and Aleva, 1990; Thomas, 1994; Tardy and Roquin, 1998; Valeton, 1999; see also Beauvais and Chardon, 2013).

Since Deccan Traps extrusion ~ 65 Ma ago, the surface of the Indian peninsula was shaped by combined or alternating chemical weathering and mechanical erosion processes that resulted in composite landscapes made of stepped lateritic paleolandsurfaces remnants of various generations occurring on either side of the Western Ghats Escarpment (WGE) (e.g., Widdowson, 1997; Gunnell, 1998). This escarpment was carved both into Deccan Traps and Precambrian basement rocks and separates a western lowland from a dissected hinterland also known as the Mysore plateau (Radhakrishna, 1993; Gunnell, 1998; Widdowson and Gunnell, 1999).

Time constraints on the formation of South Indian laterites are still poorly documented (Schmidt et al., 1983; Krishna Rao et al., 1989a) although Late Paleogene $^{40}Ar/^{39}Ar$ ages of supergene K-Mn oxides have been recently obtained from the Sandur Mn-ore deposit on the highland (Bonnet et al., 2014). Most south Indian Mn-ore deposits result from supergene weathering of late Archean supracrustal rocks, either on

73 the highland in the Sandur and Shimoga areas (Krishna Rao et al., 1982; Mohapatra et
74 al., 1996), or in the lowland at the foot of the WGE (Dessai, 1985; Fig. 1). In both
75 contexts, Mn-ore deposits are hosted by lateritic weathering profiles underlying
76 remnants of several generations of paleosurfaces, which are preserved at variable
77 elevations (Fig. 2). All these Mn-ore deposits contain K-rich Mn oxides such as
78 cryptomelane [$K_x\ Mn_{8-x}^{IV}\ Mn_x^{III}\ O_{16}$], which is datable by $^{40}Ar/^{39}Ar$ geochronology.
79 Absolute dating of K-Mn oxides generally documents periods of intense lateritic
80 weathering controlled by specific paleoclimatic conditions and as such may be used to
81 reconstruct and quantify the long-term morphoclimatic evolution of tropical shield
82 surfaces (Beauvais et al., 2008; Beauvais and Chardon, 2013; Vasconcelos, 1999b;
83 Vasconcelos and Conroy, 2003). Here we report on $^{40}Ar/^{39}Ar$ geochronological data
84 series obtained on Peninsular India that bracket three Cenozoic weathering periods and
85 constrain the tempo of long-term South Indian morphogenesis. Our results also
86 document divergent erosion and weathering histories across the WGE suggesting
87 installation of a dual climatic regime on either side of the escarpment after the Eocene
88 warming period.
89
90 **2. Material and methods**
91 2.1. Geological and geomorphological setting
92 South Indian laterites have been discriminated in two groups: highland laterites on
93 the plateau and lowland laterites in the western coastal plain (e.g., Widdowson and Cox,
94 1996). Remnants of three main lateritic paleolandsurfaces are reported on the highland
95 and the remnants of a lateritic pediment have been described in the lowland
96 (Widdowson, 1997; Gunnell, 1998; Widdowson and Gunnell, 1999). Our field

observations indicate that each highland relict paleolandsurface has a specific regolith covers. The relicts of the first, highest and oldest landsurface are capped by a weathering profile topped by an Al-Fe duricrust (Figs. 2). This duricrust is commonly economic-grade bauxite such as those preserved on the Deccan Traps (Valeton, 1999). The bauxites are also preserved on the highest topographic massifs of the southern part of the Peninsula (e.g., Londa, Bababudan, Shevaroy, Nilgiris and Palni hills; Figs. 1 and 2). Remnants of a second younger landsurface are found downslope Al-Fe duricrust relicts. They are capped by weathering profiles topped by a Fe duricrust or by a Fe-Mn duricrust if an underlying Mn-protore is present (Fig. 2). The third and last lateritic paleolandsurface on the highland is a pediment, which is capped by reworked debris of lateritic duricrusts (Fig. 2). The debris may be cemented to form a ferricrete, or a Fe-Mn duricrust, if Mn ore debris are also included in the pediment sedimentary cover above a Mn-protore (see below). Following weathering and abandonment of the pediment, the lateritic covers of the highland have been essentially stripped and incised by rivers, leaving only sparse relicts of the three paleolandsurfaces (Radhakrishna, 1993). The lowland pediment is underlain by a weathering profile that locally hosts bauxite and Mn ore pockets and is capped by a ferricrete, which may be a Fe-Mn duricrust above Mn-protores (Beauvais et al., 2016).

Four Mn-ore deposits were visited and sampled on the highland and three in the lowland (Fig. 1). Two actively operated Mn-ore deposits (Kappataswamy and Channanghi KMK-E) were sampled in the highland Sandur massif (Figs. 1 and 2b; stars 1 and 2; Table 1). Lateritic Mn-ore deposits developed upon Late Archean protores younger than 2651 ± 18 Ma, as constrained by SHRIMP U-Pb dating of their stratigraphically underlying volcanics (Nutman et al., 1996). The protores include

121 phyllites, argillites, arenites and Fe-Mn stromatolitic carbonates that yielded a 2475 ±
122 65 Ma Pb-Pb isochron age (Chadwick et al., 1996; Russell et al., 1996). The open pits
123 are weathering profiles excavated into a remnant of the second paleolandsurface capped
124 by a Fe-Mn duricrust, at 1012-1015 m elevation (Figs. 2b; 3a and 3b). A remnant of the
125 first paleolandsurface dominates the deposit at ca. 1100 m elevation (Fig. 2b).
126 Highland samples were also collected closer to the WGE, in two abandoned mines
127 of the Shimoga area (Triveni and Kumsi Mn ore open pits; Figs. 1 and 2a, stars 3 and 4,
128 respectively, see also 3c-d and Table. 1). In these pits, the protore is a metavolcanic
129 rock belonging to the Shimoga greenstone belt (Rb-Sr isochron age of 2520 ± 62 Ma;
130 Bhaskar Rao et al., 1992). The protore also comprises Mn-phyllites, which weathered
131 during the Cenozoic as constrained by palynological analyses (Krishna Rao et al.,
132 1982). The Triveni Mn ore samples (Fig. 2a) have been collected at altitudes between
133 850 and 875 m (Table 1) in the Fe-Mn duricrust-capped weathering profile of the
134 second paleolandsurface (Fig. 2a). The Kumsi pit exposes a 21 m thick lateritic profile
135 of a relict of the pediment forming the third highland paleolandsurface (~ 710 m
136 altitude; Figs. 2a and 3d). The sampled profile consists in a ~ 6 m thick dismantled
137 lateritic duricrust hosting a ~ 2 m thick sedimentary layer mixing decimetric
138 ferruginous, manganiferous clasts and infracentimetric oolites (Fig. 3d) upon ~ 15 m of
139 massive Mn-ore.
140 The weathering profile of the lowland pediment developed upon greenstones
141 similar to those of the Shimoga belt (Dessai, 1985; Fig. 1) and were constrained by
142 paleomagnetism as “late Paleogene to Neogene” in age by Schmidt et al. (1983). The
143 elevation of the pediment varies from 200 m at the foot of the WGE to 50 m close to the
144 coastline (Fig. 2c). We collected samples in four pits excavated in the pediment capping

145 ferricrete (Caurem, star 5, Naveli 1 and Naveli 2, star 6, and Cudnem, star 7; Figs. 1 and
146 2c; see also Table. 1). Caurem, Naveli 1&2 and Cudnem pits have been excavated
147 where the ferricrete lies at 100 m, 140 m and 50 m elevation, respectively. In those pits,
148 the weathering profile is 25 to 100 m thick and the ferricrete is made of cemented
149 reworked lateritic clasts (Figs. 3e-f-g; Babu, 1981; Bonnet, 2015).
150
151 2.2. Samples preparation, characterization and analysis
152 Potassium-rich end-member of coronadite group (i.e., cryptomelane) from the
153 hollandite supergroup (Biagioni et al., 2013), is a common supergene Mn-oxide of the
154 lateritic Mn-ore deposits of southern India (e.g., Krishna Rao et al., 1982; Mohapatra et
155 al., 1996) which can be used for $^{40}Ar/^{39}Ar$ dating. The crystallographic system of this
156 mineral allows argon gas retentiveness in a tunnel-type crystal lattice, which is
157 characterized by a double chain of MnO_6 octahedra and K^+ cations in the large tunnel
158 lacuna to insure the electronic neutrality of the lattice (Turner and Buseck, 1979; Post
159 and Burnham, 1986). Tunnel oxides retained efficiently Ar and K and remain close in
160 supergene environmental conditions (Vasconcelos, 1999b; Vasconcelos et al., 1994),
161 leading to meaningful crystallization age of the minerals. However K-rich Mn-oxides
162 are usually mixed with other oxides, such as others Mn-oxides (e.g., pyrolusite,
163 lithiophorite) and Fe-oxides (hematite, goethite). Therefore, careful observations and
164 extraction techniques are required to ensure meaningful dating.
165 The method implemented to characterize and separate the K-rich Mn-oxides
166 grains from field samples is summarized in figure 4. Field samples were cut with a
167 circular saw (1.5 mm breadth) to get a section allowing accurate observations. A 200-
168 300 µm thick polished thin section and a symmetrical 500 µm thick slab were made

169 from each sawed fragment. Polished thin sections have been studied using reflected
170 light microscopy (Fig. 5a-g). We also used elemental cartography by X-ray micro-
171 fluorescence (µ-XRF) with a XGT7000 Horiba Jobin Yvon producing a high-intensity
172 beam with a 100 µm spot size, Rh X-ray tube, accelerating voltage of 30 kV and current
173 of 1mA. Micro-XRF elemental maps of Fe, K and Mn are stacked together on a single
174 image using ImageJ software by assigning a distinct color to each elemental map (Figs.
175 4 and 6). The resulting images are helpful to locate K-rich phases on the slab. Electron
176 Probe Micro-chemical Analysis (EPMA) of minerals using a CAMECA SX-100
177 electron microprobe equipped with five wavelength-dispersive X-ray spectrometers
178 (WDS) provided the precise micro chemical composition of K-Mn oxides.
179 Grains were then separated from the slabs using a micro-drill under a large
180 magnifier (Fig. 4). Some of them were observed with a scanning electron microscope
181 (SEM, Fig. 5h), other were crushed to produce a powder sieved at 64 µm, which was
182 analyzed by XRD using a Panalytical X'Pert Pro MPD with a Co Kα X-ray source (λ =
183 1.79 Å) operating at 40kV and 40 mA. The remaining grains were ultrasonically
184 cleaned in absolute ethanol, conditioned in aluminum foil packets and placed into a
185 irradiation vessel along with $^{40}Ar/^{39}Ar$ dating standard Taylor Creek Rhyolite sanidine 2
186 (TCRs-2) monitor, dated at 28.608 ± 0.033 Ma (Renne et al., 2011). Irradiation took
187 place in the TRIGA Mark-II reactor of Pavia University (Italy) during 50 hours. Prior
188 experiments have shown none or very little ^{39}Ar recoil from those grains.
189 Isotopic analyses were then performed on irradiated K-rich Mn-oxide separates
190 using either step heating degassing under a CO_2 laser probe coupled with an Argus VI
191 multicollection mass spectrometer (with 4 faradays for masses ^{40}Ar-^{37}Ar and ion
192 counting on ^{36}Ar) or a step-wise heating procedure in a double vacuum Staudacher-type

193 furnace coupled with a VG3600 mass spectrometer using peak jumping and
194 Faraday/Daly analyzer as described by Arnaud et al. (2003). Mass discrimination of
195 machines and blank levels are followed daily. Isotopic ratios were corrected for
196 irradiation interferences and air contamination using a mean air value of 298.56 ± 0.31
197 (Lee et al., 2006; Renne et al., 2009).

198 Ages were statistically analyzed in three ways: ^{39}Ar release spectra, inverse
199 isochrons (Table. 2) and age's frequency or probability plots. Age spectra detail the
200 homogeneity of argon released and age stability throughout the degassing process, with
201 the prior assumption of atmospheric correction for inherited argon. When apparent ages
202 are integrated over continuous steps overlapping at the 2σ level and releasing at least
203 70% $^{39}Ar_K$, the derived plateau age is statistically robust and meaningful (e.g., Beauvais
204 et al., 2008). However, when plateau is derived from less than 70% of $^{39}Ar_K$ released
205 (e.g., Vasconcelos, 1999a; Li and Vasconcelos, 2002; Vasconcelos and Conroy, 2003;
206 Colin et al., 2005), the critical value of 50% $^{39}Ar_K$ released is accepted to calculate a
207 "plateau age" (e.g., Li et al., 2007; Feng and Vasconcelos, 2007; Vasconcelos et al.,
208 2013; Riffel et al., 2014; Bonnet et al., 2014; Deng et al., 2016) provided that it is
209 integrated over three or more continuous steps whose ages overlap at the 2σ level (Fleck
210 et al., 1977; Maluski, 1985; McDougall and Harrison, 1999). When more than two
211 apparent steps overlaps at the 2 σ level but integrate only 40 to 50% of the $^{39}Ar_K$
212 released, "pseudo plateau" are defined and considered as acceptable and meaningful
213 (Vasconcelos et al., 2013; Riffel et al., 2014).

214 When those criteria are not satisfied but barely missed (ages do not strictly
215 overlap at the 2 σ level) a "forced plateau" integrating more than two consecutive
216 reasonably flat steps is calculated with a weighed mean (weighed by the error and the

217 ^{39}Ar released in each step) (see Feng and Vasconcelos, 2007; Vasconcelos et al., 2013;
218 Riffel et al., 2014). The ^{36}Ar/^{40}Ar vs. ^{39}Ar/^{40}Ar correlation diagrams (also called inverse
219 isochrons) are also used to derive the best-fitted inverse isochron (Roddick et al., 1980)
220 allowing to estimate a statistically robust age. The inverse isochron approach also is
221 particularly useful to detect different contamination from various excess or inherited
222 argon reservoirs, which may result from atmospheric argon incorporated in the less
223 retentive site of the grain, or excess ^{40}Ar released from older K-bearing minerals. For
224 some authors (De Putter et al., 2015), best inverse isochrons exclude the first heating
225 steps, which are usually dominated by trapped atmospheric Ar in the less retentive
226 crystalline sites. These ages are derived from best-fitted inverse isochrons that should
227 have mean square weighted deviation (MSWD) as close as possible to 1 with regard to
228 the distribution of points and their absolute error, but this value is not a limitation to
229 derive an acceptable inverse isochron. Regressions are classically accepted as
230 significant when MSWD is less than 2.5 (Roddick et al., 1980), possibly around 1.
231 There is therefore a complicated trade-off between the number of points used, the
232 MSWD, and the use of the most radiogenic ^{40}Ar* rich steps.
233
234 **3. Results and interpretations**
235 3.1. Petrological and geochemical characterization
236 Descriptions of samples and K-Mn oxide grains are compiled in the table 1. Two
237 main petrographic forms of manganese ore can be distinguished. Float (very porous) or
238 platty Mn-ores show the original banding of the siliceous phyllitic protore (Figs. 3a and
239 5a; Mishra, 1978; see also Bonnet et al., 2014). Mn-ore can also be massive podiform
240 and botryoidal filling micro porosities (Fig. 5b and Fig. 6a-b) and larger cavities, in

241 which geodes formed by successive overgrowth of colloidal microstructures (Fig. 5e-f
242 and Fig. 6a) becoming massive cryptocrystalline when cavities are totally filled (Fig.
243 5b-c). Colloidal overgrowth around nucleus (e.g. iron oxide, clasts) can also form
244 massive nodules where the initial protore structure is totally erased (Fig. 5d-e).
245 Cryptomelane EPMA data are plotted in a ternary diagram (Fig. 7; see also the
246 data repository DR1). Cryptomelane from Shimoga and Goa is enriched in aluminum
247 (Fig. 7). The differences in alumina result either from contrasted parent rocks
248 composition (e.g., carbonates without alumina vs. aluminous metavolcanic phyllites) or
249 possible intergrowth with lithiophorite (Fig. 5e-g and Fig. 6a) or even gibbsite (Fig. 5h).
250 These differences may also indicate a better maturation of Sandur's cryptomelane rich
251 ores (Fig. 6), which are devoid of aluminous impurities (e.g., Beauvais et al., 1987).
252
253 3.2. Deciphering the $^{40}Ar/^{39}Ar$ age spectra
254 The different types of ^{39}Ar release spectra are shown in figures 8 and 9. Many
255 samples yielded a regular flat age spectrum (Fig. 8a). As explained above, plateau ages
256 are validated when at least three consecutive steps comprising up to 50% of total $^{39}Ar_K$
257 released overlap at the 2σ confidence level.
258 Degasing spectra may show evidence of negligible amount of ^{39}Ar, low % $^{40}Ar^*$
259 and large amount of atmospheric ^{40}Ar in the low energy degassing steps that generally
260 increases the 2σ error of the first apparent ages (Fig. 8a). Another issue is the
261 rejuvenated ages frequently observed at low temperature steps (Fig. 8b), which can be
262 the result of a loss of $^{40}Ar^*$ from less retentive and poorly crystallized sites (see
263 (Vasconcelos, 1999b). But most of the time the apparent ages progressively reach a
264 constant value at higher temperature steps allowing definition of a plateau, which is also

265 well supported by an inverse isochron (see Fig. 8b). Sixteen samples show such a
266 degasing spectrum integrating up to 90% of the total extracted signal, and excluding
267 only the very first steps with ages lower than the plateau. These well-defined plateaus
268 are used to calculate the absolute ages of the K-Mn oxides. Generally, both the ages
269 estimated from spectra and inverse isochrons are equivalent (Fig. 8a-b, Table. 2).
270 Therefore, we choose to present our ages only with ^{39}Ar release spectra that clearly
271 show a plateau, and with both spectra and inverse isochrons when no clear plateau is
272 identified. Plateau ages (70% $^{39}Ar_K$ released) and best-fitted inverse isochrons are
273 considered as first order ages and noted (A) in figures 10, 11 and 12.
274 Some age spectra do not allow calculating a standard age plateau according to the
275 definition of Fleck et al. (1977), but only a "forced-plateau" defined from ^{39}Ar release
276 spectra encompassing four steps releasing ~ 70% (Fig. 8c). In other release spectra, a
277 probable authigenic component ages the last steps, which result in an older intermediate
278 step with several little pseudo plateaus (10 to 30 % ^{39}Ar each) of similar ages (Fig. 8d).
279 In such cases, an estimated concordant pseudo-plateau age is often supported by a valid
280 inverse isochron age (Table. 2; see also Bonnet et al., 2014). This can be a valid
281 alternative when the total amount of integrated $\%^{39}Ar_k$ is higher than 40% of the total
282 signal. But such a concordant pseudo-plateau age should also be certified by a well-
283 defined plateau age in another sample from the same weathering profile. Plateau ages
284 integrating less than 70% $^{39}Ar_K$ released, "Forced plateau", "Pseudo plateau" and
285 "concordant pseudo plateau" ages are considered as second-order ages noted (B) in
286 figures 10, 11 and 12. Nevertheless, these ages are often validated by best-fitted inverse
287 isochrons (Table 2) and are meaningful of first order weathering events.

When the age spectra present an obviously convex hump shape (Fig. 9a) the youngest and oldest apparent ages may result from a mixing between gases released from two phases (e.g., Ruffet et al., 1996; Hautmann and Lippolt, 2000; Vasconcelos and Conroy, 2003; Beauvais et al., 2008; De Putter et al., 2015). Possible argon loss from less retentive intercrystalline site could also affect these degasing patterns (Fig. 9a). The statistical analysis of both the age spectrum and the inverse isochron may help to estimate minimum and maximum ages of mixed phases (e.g., Bonnet et al., 2014). In the case of sample TRI-3a the only possible inverse isochron yields a maximum estimate of the youngest phase at ~ 11 Ma (Fig. 9a). However, this age is not validated by a well-defined plateau age from another sample of the same deposit (Fig. 11), and therefore noted (C). Most spectra with a hump-shape also show a plateau integrating at least 50% of $^{39}Ar_K$ in the intermediate energy levels but the derived age is a minimum estimate of the oldest phase (e.g., KUM-4oo, Fig. 11; see also NAV-3c and NAV-3b Fig. 12). The plateaus included in these hump-shape spectra should be considered more carefully and derived ages are noted (B), but acceptable inverse isochrons are derived (Fig. 12, Table 2). Other hump shape spectra exhibit young apparent ages forming "pseudo plateaus" in low and high energy levels with concordant ages, which bracket an older plateau age in the intermediate energy level (e.g., CAU-1a, CAU-1c, CAU-3a, CAU-2, Fig. 12, Fig. 12). The correlation diagrams for these samples point to possible inverse isochrons estimating maximum and minimum age of the youngest and oldest mixed-phases respectively (Fig. 12, Table 2). For example, the oldest phases with minimum ages ~ 22 to ~ 24 Ma (Fig. 12) are probably contaminated by youngest phases with maximum age ~ 19 to 20 Ma. These ages are noted as (B) and meaningful when derived from best-fitted inverse isochrons and/or plateau integrating at least 50% $^{39}Ar_K$.

312 On another hand, the age difference between the youngest and oldest phases is larger
313 (e.g., KPA-2.5, Fig. 10; see also CAU-1b, Fig. 12), ages estimations are too speculative
314 and only the minimum age of the oldest phase can be estimated and noted with a (C) in
315 figures 10, 11 and 12 (see also Table 2). These ages are not meaningful.
316 Other samples show "saddle shape" spectra (Figs. 9b-c) with a progressive
317 decrease of the apparent ages in the intermediate energy steps and a very large increase
318 of the ages at highest energy steps. This complex type of spectra may result from
319 significant ^{39}Ar loss by recoil and/or contamination (Turner and Cadogan, 1974;
320 Vasconcelos, 1999b; Vasconcelos and Conroy, 2003). The high energy steps suggest a
321 hypogene contaminant (Vasconcelos et al., 1994; Ruffet et al., 1996; Li and
322 Vasconcelos, 2002; Bonnet et al., 2014), which can also age the other steps (e.g., Fig.
323 9c). Most of these spectra display overestimated ages, which are not reliable
324 (Vasconcelos and Conroy, 2003). Noted that no inverse isochron is derivable, the
325 correlation diagram showing at best a mixing of inherited contaminant and supergene
326 phase (Fig. 9c).
327 The Table 2 synthetize the results and shows 24 well defined plateaus ages (>
328 70% $^{39}Ar_K$) with one best-fitted inverse isochron age noted (A). In addition 18 ages
329 noted (B) are also derived either from "plateaus" and "forced plateaus" (at least 50%
330 $^{39}Ar_K$) or from "concordant pseudo plateaus" ages and best-fitted inverse isochrons. All
331 these ages are reliable and geologically significant and have been plotted against
332 altitude, and combined with individual age probability diagram (Fig. 13a) that enhances
333 most probable weathering age peaks (Vasconcelos, 1999b).
334
335 3.3. ^{40}Ar/^{39}Ar geochronology of lateritic weathering in South India

Here we present 29 newly analyzed K-Mn oxide grains that are interpreted together with grains studied by Bonnet et al. (2014) and Beauvais et al. (2016) (Table 2 and Fig. 13a). The total analysis of 46 Mn-oxide grains provides 40 age spectra with significant geological meaning as "plateaus", "forced-plateaus", "pseudo plateau" "concordant pseudo-plateaus" or "hump shape". We present our results in three figures grouping age spectra obtained from K-Mn oxide grains of the Sandur (Fig. 10), Shimoga (Fig. 11) and Goa deposits (Fig. 12). All the ages are also presented in Table 2 including the best inverse isochron age estimates (See also data repository tables DR2 and DR3).

3.3.1. $^{40}Ar/^{39}Ar$ ages from highland Sandur Mn ore deposit

Among all the samples dated in the Sandur Mn ore deposit, 18 samples show plateau ages noted (A). The ages range from ~ 26 Ma (KMK-3) to ~ 53 Ma (KPA-8) (Fig. 10 and Table 2). Two age groups are distinguished: ~ 53 - 50 Ma and ~ 37 - 26 Ma (Fig. 10). Two spectra have a "hump shape" resulting from mixed supergene phases (Bonnet et al., 2014; Hautmann and Lippolt, 2000; Ruffet et al., 1996; Vasconcelos et al., 1995). The spectrum of sample KPA-2.5 shows a maximum apparent age ~ 46 Ma old, which is a minimum estimate of the oldest phase in the mixing. In sample KPA-12a minimum age of ~ 34 Ma noted (C) for the oldest phase is coherent with plateau ages (A) between ~ 37 Ma (KMK-3b) and ~ 32 Ma (KPA-11) (Fig. 10), which are attributed to the second weathering period. Nine grains display plateau-ages between ~ 26 and ~ 30 Ma. The high frequency of these ages is linked to the analysis of several aliquots of samples KPA-10 (4 grains) and KPA-12a (6 grains), which yielded reproducible plateaus, and also allowed quantifying the growth rate for these

cryptocrystalline colloidal structures. Grains KPA-12a1 and KPA-12a5 are separated by 12.2 ± 0.1 mm (Figs. 6 and 10) and the estimated growth rate of the massive cryptocrystalline colloidal structure is 5.7 ± 3 mm. Ma^{-1}. A mean rate of 5.0 ± 4 mm. Ma^{-1} in botryoidal overgrowth microstructure was also estimated for sample KPA-10 between grains KPA-10a and KPA-10c (Figs. 6 and 10). These rates are comparable with earlier growth rate estimates of 6.4 ± 1.2 mm. Ma^{-1} (Vasconcelos et al., 1992) or 1 to 5 mm. Ma^{-1} (Hénocque et al., 1998).

3.3.2. $^{40}Ar/^{39}Ar$ ages from highland Shimoga Mn ore deposits

The obtained ages are mostly comprised between ~ 30 and 24 Ma (Fig. 11). However, one grain (KUM-4oo) displays a spectrum with a singular hump shape, which results from a mixing of two phases (Figs. 11a-b). The "forced plateau" age at ~ 39 Ma including 58% of the total amount of ^{39}Ar released is the minimum estimate of the oldest phase and noted (B), which is also supported by the sole possible inverse isochron with a MSWD value less than 2.5 (Fig. 11b). The correlation diagram does not allow estimating an acceptable age for the youngest phase in this mixed grain (Table 2). The considered grain was picked up from a lateritic clast reworked in the lateritic pediment topping the Kumsi Mn-ore deposit (site 4 on Fig. 2a). The detrital nature of this sample and its high porosity are attested by reflected light microscopy (Fig. 5d). This suggests provenance from a lateritic Mn-duricrust previously exposed on a higher landsurface, which was dissected and eroded allowing lateritic clasts transport and deposition at lower elevations on the pediment in which the Kumsi pit is excavated. Therefore, the Kumsi pediment must be younger than 39 Ma (minimum age of the oldest phase in KUM-4oo) but older than 26 Ma (most common age of the youngest

384 phase in the same profile, Fig. 11a and Table 2). Sample TRI-3b (Fig. 11) shows a
385 middle spectrum portion with ages ranging from ~ 43 to ~ 48 Ma accounting for 70% of
386 the total ^{39}Ar released. An inherited phase seems to release gas especially at high energy
387 step heating, but when this phase started to degas at lower energy, the apparent ages at
388 intermediate heating steps are artificially aged that increases the apparent age up to ~ 48
389 Ma. The best age estimation of the supergene phase in this grain is most probably ~ 43
390 Ma but must be considered only as a maximum age estimate.
391 The release spectrum of samples KUM-3f and KUM-2 show weakly aged steps at
392 the beginning of the analysis, which possibly resulted from minor ^{39}Ar recoil (Turner
393 and Cadogan, 1974). However, the disturbance is very low and meaningful age at ~ 30
394 Ma (KUM-3f) and ~ 23 Ma (KUM-2) both by a pseudo plateau (Fig. 11a) and well-
395 constrained inverse isochrons (Fig. 11b; Table. 2). Several aliquots of samples TRI-3
396 and KUM-3a (Fig. 11) yield consistent plateau ages of 25.5 Ma and ~ 26-27.5 Ma,
397 respectively.
398
399 3.3.3. ^{40}Ar/^{39}Ar ages from lowland Goa Mn ore deposits
400 The cryptomelane ages from samples of the lowland Mn-ore deposits are
401 distributed in two main age groups. The first group comprises two-ages at ~ 47 and 45
402 Ma, obtained for two aliquots of sample NAV-3, which are probably minimum
403 estimates. The spectrum of NAV-3c allows integrating 60% of the total amount of ^{39}Ar
404 released overlapping at the 2σ error (Fleck et al., 1977) that yields a plateau age (A) of
405 47.0 ± 0.6 Ma, which is supported by the inverse isochron age (Table 2 and Fig. 12b).
406 Further evidence of early weathering around ~ 45 Ma (minimum age of NAV-3b) in the
407 lowland is supported by the spectrum and a possible inverse isochron (Fig. 12). The

spectrum of sample CAU-1b (Fig. 12) also shows a maximal apparent age at ~ 45 Ma, which is a minimum age and should be noted (C). The old ages are systematically obtained from samples collected in the deepest part of the weathering profile. Younger ages between ~ 19 Ma and ~ 24 Ma (group 2) and discrete ages at ~ 8.7 Ma and 2.5 Ma are also identified (Fig. 12). All these ages are supported by inverse isochron ages (see Table. 2).

Sample CAU-2 shows a "hump shape" explained by the probable mixing of two phases, with a minimum age of ~ 24.5 Ma for the oldest and a maximum estimate of ~ 19 Ma for the youngest. The oldest estimate cannot be validated by inverse isochrons (Fig. 12b, and Table 2). In three similar cases, secondary pseudo-plateaus at ~ 20 Ma can be detected on either side of a plateau or a "forced plateau" (e.g., CAU-2). For example, sample CAU-3a (Fig. 12) shows a plateau at ~ 24 Ma, which is a minimum estimate flanked by small concordant pseudo-plateaus at ~ 19-20 Ma in low- and high-energy steps accounting together for 32% ^{39}Ar degassed. Sample aliquots CAU-1a and CAU-1c (Fig. 12) also show similar "hump shape" type spectra with a plateau age flanked by concordant pseudo-plateau ages suggesting mixing of two phases of different ages (Vasconcelos et al., 1995; Ruffet et al., 1996; Hautmann and Lippolt, 2000) but close enough to be grouped in the same weathering period ca. 19 to ca. 24 Ma. However, for these last three samples the difference between the oldest and the youngest phase (20 Ma) is small enough to allow deriving three minimum plateaus ages noted (B) at ~ 24 Ma associated with three concordant (B) maximum ages at ~ 20 Ma (Fig. 12). The youngest ages ~ 20 Ma are rather well supported by reliable inverse isochron ages (Table. 2, Fig. 12b).

3.3.4. Interpretation of the $^{40}Ar/^{39}Ar$ ages

The first- and second order (A and B) $^{40}Ar/^{39}Ar$ ages allow defining three main lateritic weathering periods (W1, W2a and W2b) in South India (Fig. 13a). The first weathering period W1 (ca. 53 to ca. 45 Ma) corresponds to intense chemical rock weathering upon both the highland and the lowland. Intense (bauxitic) weathering of the first paleolandsurface is interpreted as correlative to this weathering period (Bonnet et al., 2014; Krishna Rao et al., 1989b). The second weathering period W2 from ca. 37 to ca. 19 Ma may be divided in two stages, W2a (ca. 37-26 Ma) mostly in the highland (Sandur, ca. 37-26 Ma and Shimoga, ca. 30-26 Ma) and W2b (ca. 26-19 Ma) only in the western highland (Shimoga, ca. 26-23 Ma) and in the lowland (Goa, ca. 24-19 Ma). The early stage (W2a) characterizes late Eocene to late Oligocene lateritic weathering of the second highland paleolandsurface, as best recorded in the eastern part (Sandur), and more discretely in Shimoga (e.g., ca. 30 Ma from KUM-3f, Fig. 11b). This weathering period also led to maturation of the previously formed bauxitic weathering profiles (e.g., Krishna Rao et al., 1989b). After 26 Ma, the Sandur remnants of the two oldest paleolandsurfaces do not seem to be longer subject to weathering, while the western highland landscape (Shimoga) still weathered until ca. 23 Ma at the time the lowland weathered too. Two later minor Late Neogene weathering pulses are also recorded in the lowland (9 and 2.5 Ma).

The weathering periods would sign installation of wet and warm climate leading to thick soil development under rainforest conditions over the peninsula, whereas the time intervals between these weathering periods may be interpreted as episodes of subdued chemical weathering and correlative higher mechanical erosion and landscape dissections (e.g., Beauvais and Chardon, 2013). Such climate driven erosion processes

456 changes have resulted in the installation and preservation of the successive lateritic
457 paleolandsurfaces over South India. The first, bauxitic paleolandsurface, was essentially
458 shaped until a maximum age of ca. 45 Ma by intense weathering and only slightly
459 reworked and dissected after that time during the shaping, and later weathering of the
460 second landsurface between ca. 37 and ca. 26-23 Ma. Finally, abandonment / dissection
461 of the highland pediment after ca. 23 Ma indicates that the thick lateritic covers of
462 South India formed in the Eocene and Oligocene and that stripping of that material and
463 intense dissection of the peninsula essentially took place in the Neogene (i.e., after 23
464 Ma).
465
466 **4. Morphoclimatic implications of $^{40}Ar/^{39}Ar$ dating**
467 Periods of intense weathering have affected the highland landscapes during the
468 early Eocene, and from late Eocene to late Oligocene. By contrast, the lowland
469 weathered mostly during the early Eocene and the early Miocene (Fig. 13a). The
470 successive Eocene to early Miocene weathering periods documented by the present
471 study coincided with the northward migration of India across the humid equatorial belt
472 (Fig. 13b). Early Eocene bauxitic weathering also coincided with the Eocene climatic
473 optimum (Fig. 13c), at a time of relatively high atmospheric CO_2 (Pearson and Palmer,
474 2000), North Atlantic rifting (62 to 55 Ma) and the subduction of Tethysian carbonates
475 (Van der Voo et al., 1999).
476
477 4.1. Early Eocene lateritic weathering (ca. 53-45 Ma; W1)
478 The $^{40}Ar/^{39}Ar$ ages indicate that lateritic weathering started at least ~ 50 Ma ago
479 over the highland and ~ 47 Ma in the lowland (Figs. 10, 12 and 13a). Preserved laterites

as old as 47 Ma under the lowland pediment argue for Early Eocene installation and stabilization of the Western Ghats Escarpment with a lateritic pediment on its piedmont (Beauvais et al., 2016). The old ages (ca. 53 to ca. 45 Ma) also document synchronous lateritic weathering in the lowland and the highland (Beauvais et al., 2016), when India drifting slowed down at the onset of the collision with Asia ~ 50 Ma ago (e.g., Zhu et al., 2005; Rowley and Currie, 2006). In the meantime, India also entered a latitudinal range where water precipitation was higher than evaporation (Fig. 13b) propitious to the development of equatorial and/or tropical warm and humid forest (Kent and Muttoni, 2008; see also Patriat and Achache, 1984; Manabe and Bryan, 1985; Tardy and Roquin, 1998; Chatterjee et al., 2013) that further enhanced lateritic weathering. At the time of India-Asia collision, CO_2 degassing of pelagic carbonate into the atmosphere ceased with the end of the North Tethys subduction (Caldeira, 1992) concomitantly with intense continental (bauxitic) lateritic weathering worldwide (Prasad, 1983; Valeton, 1999; Retallack, 2010) and correlative offshore carbonate production (e.g., Chaubey et al., 2002 for the West Indian margin). Bauxitic weathering was effectively documented by $^{40}Ar/^{39}Ar$ cryptomelane ages throughout the tropical belt during the Eocene e.g., from 56 to 51 Ma in South America (Ruffet et al., 1996; Vasconcelos, 1999b; Vasconcelos et al., 1994) and from 59 to 45 Ma in West Africa (Hénocque et al., 1998; Colin et al., 2005; Beauvais et al., 2008). Combined together, all these concomitant phenomena consumed high quantities of atmospheric CO_2 (Dessert et al., 2003) that progressively cooled the climate once past the Eocene Climatic Optimum (Kent and Muttoni, 2008, 2012; see also Zachos et al., 2001, 2008). In turn, progressive climate cooling from Mid-Eocene onward (Fig. 13c) has favoured the dissection of early Eocene bauxitic landscapes.

504

505 4.2. Late Eocene-late Oligocene weathering (ca. 37-26 Ma; W2a)

506 This first weathering stage of period W2 is marked mostly in the highland,
507 particularly by two prominent peaks at ~ 28 Ma and ~ 26 Ma in the Sandur massif and
508 the Shimoga area, respectively (Fig. 13a), and more speculatively in the lowland if we
509 consider that 24 Ma is a minimum age. This episode (37-26 Ma) is interpreted to reflect
510 the continental weathering response to the late Oligocene warming (Fig. 13c) at a time
511 of a marine transgression propitious to offshore carbonate production (Biswas, 1987).
512 Thickening of the proto-Himalaya since ~ 40 Ma (Aikman et al., 2008) resulted in the
513 installation of an orographic barrier (Molnar et al., 1993; Ramstein et al., 2005), which
514 redistributed the humid air masses southward (Dupont-Nivet et al., 2008). A monsoonal
515 regime installed at that time in Southern Asia (Licht et al., 2014) that could intensify
516 weathering processes on the Indian peninsula. Under such climatic conditions, the
517 lateritic weathering profiles underlying remnants of the first two paleolandsurfaces
518 became less well drained as a result of river incision, but did not become totally
519 inactive, as attested by younger dates in Sandur, e.g., ca. 37 to ca. 26 Ma (Figs. 10 and
520 13a). During this period, the early Eocene bauxites have still evolved on the highland
521 (Krishna Rao et al., 1989b; see also Bonnet et al., 2014) at least until global cooling by
522 ~ 34 Ma (Fig. 13c; Molnar and England, 1990; Zachos et al., 2001).

523 Early Oligocene cooling also coincided with a sea level fall (Chaubey et al.,
524 2002), and the installation of dryer climatic conditions (see Fig. 13c), which may have
525 resulted in the attenuation of the weathering intensity observed between 32 and 29 Ma
526 in the highland (Fig. 13a). The highland pediment may possibly have been formed in
527 this time interval, and subsequently weathered between 29 and 23 Ma. At that time, the

lowland landscape was also possibly rejuvenated, but previously formed lateritic weathering mantles as old as ca. 47-45 Ma were preserved (Figs. 12 and 13a), attesting to a very slow denudation regime of the pediment below the WGE (Beauvais et al., 2016). The contrasted weathering record of the highland and the lowland after the Mid-Eocene (Fig. 13a) suggests a spatial contrast in rainfall distribution on either side of the WGE. This contrast was mostly controlled by dominant South-East moisture fluxes during the late Eocene and the early Oligocene (Licht et al., 2014; Chen and Li, 2014) before installation of modern monsoon regimes in the early Miocene (Clift et al., 2008), which reactivated weathering preferentially in the lowland.

4.3. Late Oligocene-Early Miocene weathering (ca. 26-19 Ma; W2b)

This second stage of weathering period W2 is mostly marked in the western highland and the lowland. Weathering in eastern highland lateritic profiles of the Sandur massif definitively ceased at ca. 26 Ma (Bonnet et al., 2014), while the western part of the highland adjacent to the WGE (Shimoga) possibly weathered until ca. 23 Ma (Fig. 13a). Therefore, the highland lateritic pediment carrying those profiles has been incised essentially after 23 Ma at a rate < 5 m/m.y. (Figs. 2a-b). During highland incision, lateritic weathering was reactivated on the lowland pediment with a peak activity at ~ 19-21 Ma (Fig. 13a). Central Asia aridification started ~ 24 Ma ago (Sun et al., 2010). Highland weathering mitigation after ~ 23 Ma may be due to such a change in climatic regime, which increased the east-west wetness gradient over peninsular India and signed the onset of modern-like monsoonal regimes (Clift et al., 2008; see also Chatterjee et al., 2013).

551 The lack of reliable ages between ~ 19 Ma and 9 Ma (Fig. 13a) suggests that
552 weathering is not recorded or preserved in peninsular India during Mid-Miocene. After
553 the early Miocene (i.e., after ca. 16 Ma), a significant change has been however
554 observed in the clay content of sediments from the neighbouring Arabian Sea, wherein
555 illite became dominant compared to kaolinite and smectite (Phillips et al., 2014). This,
556 together with our results, indicates an attenuation of continental weathering and
557 suggests dominant landscape dissection of the highland. By contrast, the lowland
558 lateritic pediment was only slightly dissected after ~ 19 Ma (Beauvais et al., 2016). The
559 weathering pulses at ~ 9 Ma and ~ 2.5 Ma (Figs. 12 and 13a) may be linked to Late
560 Neogene intensification of the Asian monsoon in the sub region (Zhisheng et al., 2001),
561 which may have been driven by uplift of the Tibetan plateau (Molnar et al., 1993; see
562 also Clift et al., 2008).
563
564 **5. Conclusion**
565 The $^{40}Ar/^{39}Ar$ dating of supergene cryptomelane formed *in situ* in lateritic
566 weathering profiles of Peninsular India sheds light on the Cenozoic weathering and
567 erosion history of the subcontinent's surface. Cryptomelane ages document three major
568 periods of weathering, i.e., early Eocene (W1) both on the highland and the lowland, ~
569 late Eocene – late Oligocene (W2a), only in the highland, and early Miocene (W2b),
570 mostly in lowland. The $^{40}Ar/^{39}Ar$ age series suggest subdued relief production and
571 dominant weathering of the highland before ~ 23 Ma and its dissection and stripping
572 after that time, while the lowland weathered in the Early Eocene and Miocene before
573 being slightly incised after ~ 19 Ma. The oldest ages (53-45 Ma) indicate widespread
574 Eocene lateritic weathering in South India at the time of global Eocene climatic

optimum, when the peninsula crossed the equatorial belt. Our results also document the installation of a dual climatic regime across the Western Ghats escarpment after the Eocene climatic optimum, leading to divergent weathering and erosion patterns on both sides of this topographic barrier. Hence, K-Mn oxides $^{40}Ar/^{39}Ar$ age series document the tempo of South Indian morphogenesis, and as such may be viewed as a proxy for erosion and climatically driven weathering over geological time scales.

Acknowledgements- This work was funded by Indo-French Centre for the Promotion of Advanced Research (IFCPAR) project 5007-1, the IRD (UR 161) and the CNRS (INSU 2011-CT2). The French Ministry for the Scientific Research and Education granted N.J. Bonnet a Ph.D. scholarship (ED251, Aix Marseille Université, Observatoire des Sciences de l'Univers Pytheas). N.J. Bonnet was also supported by a fellowship from IFCPAR. We thank L. Giosan and an anonymous referee for their comments and suggestions, and editorial handling from F. Chabaux and Michael E. Böttcher.

References

Aikman, A.B., Harrison, T.M., Lin, D., 2008. Evidence for Early (> 44 Ma) Himalayan Crustal Thickening, Tethyan Himalaya, southeastern Tibet. Earth Planet. Sci. Lett. 274, 14–23. doi:10.1016/j.epsl.2008.06.038

Arnaud, N., Tapponier, P., Roger, F., Brunel, M., Scharer, U., Wen, C., Xu, Z., 2003. Evidence for Mesozoic shear along the western Kunlun and Altyn-Tagh fault, northern Tibet (China). J. Geophys. Res. 108, 2053. doi:10.1029/2001JB000904

598 Babu, P.V.L.P., 1981. Laterite as an unconformity plane in the evolution of the South
599 Indian peninsula – a synthesis. In: International Seminar on Lateritisation
600 Processes (Trivandrum, India 11-14 December, 1979). Balkema, Rotterdam,
601 Netherlands pp. 302–307.
602 Bárdossy, G., Aleva, G.J.J., 1990. Lateritic bauxites. In: Developments in Economic
603 Geology (27). Elsevier, Amsterdam, Netherlands, pp. 624.
604 Beauvais, A., Bonnet, N.J., Chardon, D., Arnaud, N.O., Jayananda, M., 2016. Very
605 long-term stability of passive margin escarpment constrained by $^{40}Ar/^{39}Ar$
606 dating of K-Mn oxides. Geology 44, 299-302. doi:10.1130/G37303.1
607 Beauvais, A., Chardon, D., 2013. Modes, tempo, and spatial variability of Cenozoic
608 cratonic denudation: The West African example. Geochem. Geophys.
609 Geosystems 14, 1590–1608.
610 Beauvais, A., Melfi, A., Nahon, D., Trescases, J.J., 1987. Pétrologie du gisement
611 latéritique manganésifère d'Azul (Brésil). Min. Deposita 22, 124–134.
612 doi:10.1007/BF00204689
613 Beauvais, A., Ruffet, G., Hénocque, O., Colin, F., 2008. Chemical and physical erosion
614 rhythms of the West African Cenozoic morphogenesis: The ^{39}Ar-^{40}Ar dating of
615 supergene K-Mn oxides. J. Geophys. Res. Earth Surf. 113, F04007.
616 doi:10.1029/2008jf000996
617 Bhaskar Rao, Y., Sivaraman, T., Pantulu, G., Gopalan, K., Naqvi, S., 1992. Rb-Sr ages
618 of late Archean metavolcanics and granites, Dharwar craton, South India and
619 evidence for Early Proterozoic thermotectonic event (s). Precambrian Res. 59,
620 145–170. doi:10.1016/0301-9268(92)90055-S

621 Biagioni, C., Capalbo, C., Pasero, M., 2013. Nomenclature tunings in the hollandite
622 supergroup. Eur. J. Mineral. 25, 85–90. doi:10.1127/0935-1221/2013/0025-2255
623 Biswas, S.K., 1987. Regional tectonic framework, structure and evolution of the
624 western marginal basins of India. Tectonophysics 135, 307–327.
625 doi:10.1016/0040-1951(87)90115-6
626 Bonnet, N.J., 2015. Dynamique long-terme d'une marge continentale divergente (Les
627 Ghâts Occidentaux de l'Inde péninsulaire) : Contraintes géochronologiques
628 ^{40}Ar-^{39}Ar des paléosurfaces latéritiques. PhD thesis, Aix Marseille Université,
629 France, pp. 286
630 Bonnet, N.J., Beauvais, A., Arnaud, N., Chardon, D., Jayananda, M., 2014. First
631 ^{40}Ar/^{39}Ar dating of intense Late Palaeogene lateritic weathering in Peninsular
632 India. Earth Planet. Sci. Lett. 386, 126–137. doi:10.1016/j.epsl.2013.11.002
633 Caldeira, K., 1992. Enhanced Cenozoic chemical weathering and the subduction of
634 pelagic carbonate. Nature 357, 578–581. doi:10.1038/357578a0
635 Chadwick, B., Vasudev, V., Ahmed, N., 1996. The Sandur schist belt and its adjacent
636 plutonic rocks implications for Late Archaean crustal evolution in Karnataka. J.
637 Geol. Soc. India 47, 635–639.
638 Chardon, D., Jayananda, M., Chetty, T.R., Peucat, J.-J., 2008. Precambrian continental
639 strain and shear zone patterns: South Indian case. J. Geophys. Res. 113, B08402.
640 doi:10.1029/2007JB005299
641 Chatterjee, S., Goswami, A., Scotese, C.R., 2013. The longest voyage: Tectonic,
642 magmatic, and paleoclimatic evolution of the Indian plate during its northward
643 flight from Gondwana to Asia. Gondwana Res. 23, 238–267.
644 doi:10.1016/j.gr.2012.07.001

645 Chaubey, A.K., Gopala Rao, D., Srinivas, K., Ramprasad, T., Ramana, M..,
646 Subrahmanyam, V., 2002. Analyses of multichannel seismic reflection, gravity
647 and magnetic data along a regional profile across the central-western continental
648 margin of India. Mar. Geol. 182, 303–323. doi:10.1016/S0025-3227(01)00241-9
649 Chen, L., Li, J., 2014. $^{40}Ar/^{39}Ar$ ages and stable isotopes of supergene jarosite from the
650 Baiyin VHMS ore field, NE Tibetan Plateau with paleoclimatic implications.
651 Chin. Sci. Bull. 59, 2999–3009. doi:10.1007/s11434-014-0276-8
652 Clift, P.D., Hodges, K.V., Heslop, D., Hannigan, R., Van Long, H., Calves, G., 2008.
653 Correlation of Himalayan exhumation rates and Asian monsoon intensity. Nat.
654 Geosci. 1, 875–880. doi:10.1038/ngeo351
655 Colin, F., Beauvais, A., Ruffet, G., Hénocque, O., 2005. First $^{40}Ar/^{39}Ar$ geochronology
656 of lateritic manganiferous pisolites: Implications for the Palaeogene history of a
657 West African landscape. Earth Planet. Sci. Lett. 238, 172–188.
658 doi:10.1016/j.epsl.2005.06.052
659 Deng, X.-D., Li, J.-W., Vasconcelos, P.M., 2016. $^{40}Ar/^{39}Ar$ dating of supergene Mn-
660 oxides from the Zunyi Mn deposit, Guizhou Plateau, SW China: implications for
661 chemical weathering and paleoclimatic evolution since the late Miocene. Chem.
662 Geol. *in press* doi:10.1016/j.chemgeo.2016.02.009
663 De Putter, T., Ruffet, G., Yans, J., Mees, F., 2015. The age of supergene manganese
664 deposits in Katanga and its implications for the Neogene evolution of the
665 African Great Lakes Region. Ore Geol. Rev. 71, 350–362.
666 doi:10.1016/j.oregeorev.2015.06.015
667 Dessai, A., 1985. An appraisal of the manganese ore deposits of Goa, India. Proc.
668 Indian Natl. Sci. Acad. Part Phys. Sci. 51, 1021–1032.

669 Dessert, C., Dupré, B., Gaillardet, J., François, L.M., Allègre, C.J., 2003. Basalt
670 weathering laws and the impact of basalt weathering on the global carbon cycle.
671 Chem. Geol. 202, 257–273. doi:10.1016/j.chemgeo.2002.10.001
672 Dupont-Nivet, G., Hoorn, C., Konert, M., 2008. Tibetan uplift prior to the Eocene-
673 Oligocene climate transition: Evidence from pollen analysis of the Xining Basin.
674 Geology 36, 987. doi:10.1130/G25063A.1
675 Feng, Y.-X., Vasconcelos, P.M., 2007. Chronology of Pleistocene weathering
676 processes, southeast Queensland, Australia. Earth Planet. Sci. Lett. 263, 275–
677 287. doi:10.1016/j.epsl.2007.08.036
678 Fleck, R.J., Sutter, J.F., Elliot, D.H., 1977. Interpretation of discordant $^{40}Ar/^{39}Ar$ age-
679 spectra of mesozoic tholeiites from antarctica. Geochim. Cosmochim. Acta 41,
680 15–32. doi:10.1016/0016-7037(77)90184-3
681 Grandin, G., 1976. Aplanissements cuirassés et enrichissement des gisements de
682 manganèse dans quelques régions d'Afrique de l'Ouest. Mém. ORSTOM (82),
683 Université de Strasbourg, Paris, France, pp. 276
684 Gunnell, Y., 1998. The interaction between geological structure and global tectonics in
685 multistoreyed landscape development: a denudation chronology of the South
686 Indian shield. Basin Res. 10, 281–310. doi:10.1046/j.1365-2117.1998.00072.x
687 Hautmann, S., Lippolt, H.J., 2000. $^{40}Ar/^{39}Ar$ dating of central European K–Mn oxides
688 — a chronological framework of supergene alteration processes during the
689 Neogene. Chem. Geol. 170, 37–80. doi:10.1016/S0009-2541(99)00241-7
690 Hénocque, O., Ruffet, G., Colin, F., Féraud, G., 1998. $^{40}Ar/^{39}Ar$ dating of West African
691 lateritic cryptomelanes. Geochim. Cosmochim. Acta 62, 2739–2756.
692 doi:10.1016/S0016-7037(98)00185-9

693 Kent, D.V., Muttoni, G., 2012. Modulation of Late Cretaceous and Cenozoic climate by
694 variable drawdown of atmospheric *p*CO2 from weathering of basaltic provinces
695 on continents drifting through the equatorial humid belt. Clim. Past Discuss. 8,
696 4513–4564. doi:10.5194/cpd-8-4513-2012
697 Kent, D.V., Muttoni, G., 2008. Equatorial convergence of India and early Cenozoic
698 climate trends. Proc. Natl. Acad. Sci. 105, 16065–16070.
699 doi:10.1073/pnas.0805382105
700 Krishna Rao, B., Muzamil Ahmed, M., Janardhana, M.R., 1989a. Age of manganiferous
701 laterite of Uttara Kanada district, Karnataka. J. Geol. Soc. India 34, 413–420.
702 Krishna Rao, B., Satish, P.N., Sethumadhav, M.S., 1989b. Syngenetic and Epigenetic
703 features and genesis of the beauxite-bearing laterite of Boknur-Navge, Belgaum
704 district, Karnataka. J. Geol. Soc. India 34, 46–60.
705 Krishna Rao, B., Srinivasan, R., Ramachandra, B.L., Sreenivas, B.L., 1982. Mode of
706 occurrence and origin of manganese ores of Shimoga district, Karnataka. J.
707 Geol. Soc. India 23, 226–235.
708 Lee, J.-Y., Marti, K., Severinghaus, J.P., Kawamura, K., Yoo, H.-S., Lee, J.B., Kim,
709 J.S., 2006. A redetermination of the isotopic abundances of atmospheric Ar.
710 Geochim. Cosmochim. Acta 70, 4507–4512.
711 Licht, A., van Cappelle, M., Abels, H.A., Ladant, J.-B., Trabucho-Alexandre, J.,
712 France-Lanord, C., Donnadieu, Y., Vandenberghe, J., Rigaudier, T., Lécuyer,
713 C., Terry, D., Adriaens, R., Boura, A., Guo, Z., Soe, A.N., Quade, J., Dupont-
714 Nivet, G., Jaeger, J.-J., 2014. Asian monsoons in a late Eocene greenhouse
715 world. Nature 513, 501. doi:10.1038/nature13704

716 Li, J.-W., Vasconcelos, P., 2002. Cenozoic continental weathering and its implications
717 for the palaeoclimate: evidence from $^{40}Ar/^{39}Ar$ geochronology of supergene K–
718 Mn oxides in Mt Tabor, central Queensland, Australia. Earth Planet. Sci. Lett.
719 200, 223–239. doi:10.1016/S0012-821X(02)00594-0
720 Li, J.-W., Vasconcelos, P., Duzgoren-Aydin, N., Yan, D.-R., Zhang, W., Deng, X.-D.,
721 Zhao, X.-F., Zeng, Z.-P., Hu, M.-A., 2007. Neogene weathering and supergene
722 manganese enrichment in subtropical South China: An $^{40}Ar/^{39}Ar$ approach and
723 paleoclimatic significance. Earth Planet. Sci. Lett. 256, 389–402.
724 doi:10.1016/j.epsl.2007.01.021
725 Maluski, H., 1985. Méthode Argon 39 - Argon 40 : Principe et applications aux
726 minéraux des roches terrestres In: Méthodes de Datation Par Les Phénomènes
727 Nucléaires Naturels - Applications. Masson, Paris, France, pp. 341–372.
728 Manabe, S., Bryan, K., 1985. CO_2-induced change in a coupled ocean-atmosphere
729 model and its paleoclimatic implications. J. Geophys. Res. 90, 689 – 707.
730 McDougall, I., Harrison, T.M., 1999. Geochronology and thermochronology by the
731 $^{40}Ar/^{39}Ar$ method, 2nd ed., Oxford University Press, New York, USA, pp. 271.
732 Mishra, R.N., 1978. Exploration planing for Sandur manganese ores. J. Geol. Soc. India
733 19, 446–453.
734 Mohapatra, B.K., Rao, D.S., Nayak, B.D., Sahoo, R.K., 1996. Mineralogical and
735 chemical characteristics of ferromanganese ores from Sandur, Karnataka, India.
736 J. Mineral. Petrol. Econ. Geol. 91, 46–61. doi:10.2465/ganko.91.48
737 Molnar, P., England, P., 1990. Late Cenozoic uplift of mountain ranges and global
738 climate change: chicken or egg? Nature 346, 29–34. doi:10.1038/346029a0

739 Molnar, P., England, P., Martinod, J., 1993. Mantle dynamics, uplift of the Tibetan
740 Plateau, and the Indian Monsoon. Rev. Geophys. 31, 357.
741 doi:10.1029/93RG02030
742 Nahon, D., 1991. Introduction to the petrology of soils and chemical weathering. Wiley-
743 Interscience, New-York, USA, pp. 313.
744 Nutman, A.P., Chadwick, B., Krishna Rao, B., Vasudev, V.N., 1996. SHRIMP U/Pb
745 zircon ages of acid volcanic rocks in the Chitradurga and Sandur Groups, and
746 granites adjacent to the Sandur Schist Belt, Karnataka. J. Geol. Soc. India 47,
747 153–164.
748 Ollier, C.D., 1988. Deep Weathering, Groundwater and Climate. Geogr. Ann. Ser. Phys.
749 Geogr. 70, 285–290. doi:10.2307/521260
750 Patriat, P., Achache, J., 1984. India–Eurasia collision chronology has implications for
751 crustal shortening and driving mechanism of plates. Nature 311, 615–621.
752 doi:10.1038/311615a0
753 Pearson, P.N., Palmer, M.R., 2000. Atmospheric carbon dioxide concentrations over the
754 past 60 million years. Nature 406, 695–699.
755 Pedro, G., 1968. Distribution des principaux types d'altération chimiques à la surface de
756 globe. Rev. Géographie Phys. Dyn. 5, 457–470.
757 Phillips, S.C., Johnson, J.E., Underwood, M.B., Guo, J., Giosan, L., Rose, K., 2014.
758 Long-timescale variation in bulk and clay mineral composition of Indian
759 continental margin sediments in the Bay of Bengal, Arabian Sea, and Andaman
760 Sea. Mar. Pet. Geol. 58, 117–138. doi:10.1016/j.marpetgeo.2014.06.018
761 Post, J.E., Burnham, C.W., 1986. Modeling tunnel-cation displacements in hollandites
762 using structure-energy calculations. Am. Mineral. 71, 1178–1185.

763 Prasad, G., 1983. A review of the early Tertiary bauxite event in South America, Africa
764 and India. J. Afr. Earth Sci. 1983 1, 305–313. doi:10.1016/S0731-
765 7247(83)80015-9
766 Radhakrishna, B.P., 1993. Neogene uplift and geomorphic rejunevation of the Indian
767 Peninsula. Curr. Sci. 64.
768 Ramstein, G., Khodri, M., Donnadieu, Y., Fluteau, F., Goddéris, Y., 2005. Impact of the
769 hydrological cycle on past climate changes: three illustrations at different time
770 scales. Comptes Rendus Geosci. 337, 125–137. doi:10.1016/j.crte.2004.10.016
771 Renne, P.R., Balco, G., Ludwig, K.R., Mundil, R., Min, K., 2011. Response to the
772 comment by W.H. Schwarz et al. on "Joint determination of ^{40}K decay constants
773 and ^{40}Ar*/^{40}K for the Fish Canyon sanidine standard, and improved accuracy for
774 ^{40}Ar/^{39}Ar geochronology" by P.R. Renne et al. (2010). Geochim. Cosmochim.
775 Acta 75, 5097–5100. doi:10.1016/j.gca.2011.06.021
776 Renne, P.R., Cassata, W.S., Morgan, L.E., 2009. The isotopic composition of
777 atmospheric argon and ^{40}Ar/^{39}Ar geochronology: Time for a change? Quat.
778 Geochronol. 4, 288–298. doi:10.1016/j.quageo.2009.02.015
779 Retallack, G.J., 2010. Lateritization and Bauxitization Events. Econ. Geol. 105, 655–
780 667. doi:10.2113/gsecongeo.105.3.655
781 Riffel, S.B., Vasconcelos, P.M., Carmo, I.O., Farley, K.A., 2015. Combined ^{40}Ar/^{39}Ar
782 and (U–Th)/He geochronological constraints on long-term landscape evolution
783 of the Second Paraná Plateau and its ruiniform surface features, Paraná, Brazil.
784 Geomorphology 233, 52–63. doi:10.1016/j.geomorph.2014.10.041

785 Roddick, J.C., Cliff, R.A., Rex, D.C., 1980. The evolution of excess argon in alpine
786 biotites — A ^{40}Ar-^{39}Ar analysis. Earth Planet. Sci. Lett. 48, 185–208.
787 doi:10.1016/0012-821X(80)90181-8
788 Rowley, D.B., Currie, B.S., 2006. Palaeo-altimetry of the late Eocene to Miocene
789 Lunpola basin, central Tibet. Nature 439, 677–681. doi:10.1038/nature04506
790 Ruffet, G., Innocent, C., Michard, A., Féraud, G., Beauvais, A., Nahon, D., Hamelin,
791 B., 1996. A geochronological ^{40}Ar^{39}Ar and ^{87}Rb^{81}Sr study of K-Mn oxides from
792 the weathering sequence of Azul, Brazil. Geochim. Cosmochim. Acta 60, 2219–
793 2232. doi:10.1016/0016-7037(96)00080-4
794 Russell, J., Chadwick, B., Rao, B.K., Vasudev, V.N., 1996. Whole-rock Pb/Pb isotopic
795 ages of Late Archaean limestones, Karnataka, India. Precambrian Res. 78, 261–
796 272. doi:10.1016/0301-9268(95)00082-8
797 Schmidt, P.W., Prasad, V., Ramam, P.K., 1983. Magnetic ages of some Indian laterites.
798 Palaeogeogr. Palaeoclimatol. Palaeoecol. 44, 185–202. doi:10.1016/0031-
799 0182(83)90102-5
800 Sun, J., Ye, J., Wu, W., Ni, X., Bi, S., Zhang, Z., Liu, W., Meng, J., 2010. Late
801 Oligocene-Miocene mid-latitude aridification and wind patterns in the Asian
802 interior. Geology 38, 515–518. doi:10.1130/G30776.1
803 Tardy, Y., 1997. Petrology of laterites and tropical soils. Balkema, Rotterdam,
804 Netherlands, pp. 408.
805 Tardy, Y., Roquin, C., 1998. Dérive des continents paleoclimats et altérations
806 tropicales. BRGM, Orléan, France, pp. 484.
807 Thomas, M.F., 1994. Geomorphology in the tropics: a study of weathering and
808 denudation in low latitudes. John Wiley & Sons, Chichester, UK, pp. 482.

809 Turner, G., Cadogan, P.H., 1974. Possible effects of ^{39}Ar recoil in ^{40}Ar-^{39}Ar dating.
810 Proc. Fifth Lunar Sci. Conf. 2, 1601 – 1615.
811 Turner, S., Buseck, P.R., 1979. Manganese Oxide Tunnel Structures and Their
812 Intergrowths. Science 203, 456–458. doi:10.1126/science.203.4379.456
813 Valeton, I., 1999. Saprolite-bauxite facies of ferralitic duricrust on paleosurfaces off
814 former Pangaea. Spec. Publ. Int. Assoc. Sedimentol. 153–158.
815 Van der Voo, R., Spakman, W., Bijwaard, H., 1999. Tethyan subducted slabs under
816 India. Earth Planet. Sci. Lett. 171, 7–20. doi:10.1016/S0012-821X(99)00131-4
817 Vasconcelos, P.M., 1999a. ^{40}Ar/^{39}Ar Geochronology of Supergene Processes in Ore
818 Deposits. In: Lambert, David D. and Ruiz, Joaquin (Eds.), Application of
819 Radiogenic Isotopes to Ore Deposit Research and Exploration. Reviews in
820 Economic Geology. Society of Economic Geologists, Boulder, CO, USA, pp.
821 73-113.
822 Vasconcelos, P.M., 1999b. K-Ar and ^{40}Ar/^{39}Ar geochronology of weathering processes.
823 Annu. Rev. Earth Planet. Sci. 27, 183–229. doi:10.1146/annurev.earth.27.1.183
824 Vasconcelos, P.M., Becker, T.A., Renne, P.R., Brimhall, G.H., 1992. Age and duration
825 of weathering by ^{40}K-^{40}Ar and ^{40}Ar-^{39}Ar analysis of supergene potassium-
826 manganese oxides. Science 258, 451–455. doi:10.1126/science.258.5081.451
827 Vasconcelos, P.M., Conroy, M., 2003. Geochronology of weathering and landscape
828 evolution, Dugald River valley, NW Queensland, Australia. Geochim.
829 Cosmochim. Acta 67, 2913–2930. doi:10.1016/S0016-7037(02)01372-8
830 Vasconcelos, P.M., Heim, J.A., Farley, K.A., Monteiro, H., Waltenberg, K., 2013.
831 ^{40}Ar/^{39}Ar and (U-Th)/He - ^{4}He/^{3}He geochronology of landscape evolution and

channel iron deposit genesis at Lynn Peak, Western Australia. Geochim. Cosmochim. Acta 117, 283–312. doi:10.1016/j.gca.2013.03.037

Vasconcelos, P.M., Renne, P.R., Becker, T.A., Wenk, H.-R., 1995. Mechanisms and kinetics of atmospheric, radiogenic, and nucleogenic argon release from cryptomelane during $^{40}Ar^{39}Ar$ analysis. Geochim. Cosmochim. Acta 59, 2057–2070. doi:10.1016/0016-7037(95)00126-3

Vasconcelos, P.M., Renne, P.R., Brimhall, G.H., Becker, T.A., 1994. Direct dating of weathering phenomena by $^{40}Ar/^{39}Ar$ and K-Ar analysis of supergene K-Mn oxides. Geochim. Cosmochim. Acta 58, 1635–1665. doi:10.1016/0016-7037(94)90565-7

Widdowson, M., 1997. Tertiary paleosurfaces of the SW Deccan, Western India: implication for passive margin uplift. In: Widdowson, M. (Ed.), Palaeosurfaces: Recognition, Reconstruction and Palaeoenvironmental Interpretation. Geological Society Special Publication, London, UK, pp. 221–248.

Widdowson, M., Cox, K.G., 1996. Uplift and erosional history of the Deccan Traps, India: Evidence from laterites and drainage patterns of the Western Ghats and Konkan Coast. Earth Planet. Sci. Lett. 137, 57–69. doi:10.1016/0012-821X(95)00211-T

Widdowson, M., Gunnell, Y., 1999. Tertiary palaeosurfaces and lateritization of the coastal lowlands of western peninsula India. In: Thiry, M., Simon-Coinçon, R. (Eds.), Palaeoweathering, Palaeosurfaces and Related Continental Deposits. International Association of Sedimentologists, Special Publication, Blackwell Science, Oxford, UK, pp. 245–274.

855 Zachos, J.C., Dickens, G.R., Zeebe, R.E., 2008. An early Cenozoic perspective on
856 greenhouse warming and carbon-cycle dynamics. Nature 451, 279–283.
857 doi:10.1038/nature06588
858 Zachos, J.C., Pagani, M., Sloan, L., Thomas, E., Billups, K., 2001. Trends, Rhythms,
859 and Aberrations in Global Climate 65 Ma to Present. Science 292, 686–693.
860 doi:10.1126/science.1059412
861 Zhisheng, A., Kutzbach, J.E., Prell, W.L., Porter, S.C., 2001. Evolution of Asian
862 monsoons and phased uplift of the Himalaya–Tibetan plateau since Late
863 Miocene times. Nature 411, 62 – 66. doi:10.1038/35075035
864 Zhu, B., Kidd, W.S.F., Rowley, D.B., Currie, B.S., Shafique, N., 2005. Age of Initiation
865 of the India-Asia Collision in the East-Central Himalaya. J. Geol. 113, 265 –
866 285. doi:10.1086/428805
867
868

869 ## Figures and table caption

870 **Figure 1.** Simplified geological map (adapted from Chardon et al., 2008) superimposed
871 to Gtopo 30 m showing the location of the Mn ore deposit pits (stars). Kappataswamy
872 pit (Star 1); Channanghi KMK-East pit (star 2); Triveni pit (star 3); Kumsi pit (star 4);
873 Caurem pit (star 5); Naveli 1 & 2 pits (star 6); Cudnem pit (star 7). Offshore bathymetry
874 is from ETOPO1 (1.8 km).
875
876 **Figure 2.** Synthetic topographic sections with major lateritic weathering surface relics.
877 **(a) (b)** sections located located in the figure 1. **(c)** Detailed section across the lowland
878 pediment. The stars and numbers are the sampled open pits located in the figure 1.

879

880 **Figure 3**. Sampled lateritic weathering profiles. **(a)** Kappataswamy, **(b)** Channanghi
881 KMK-E, **(c)** Triveni, **(d)** Kumsi, **(e)** Cudnem, **(f)** Caurem and **(g)** Naveli 1. White
882 crosses show the sampling spots. (See table 1 for GPS locations and ore sample types)
883

884 **Figure 4**. Synthetic sketch of the different steps of preparation, observation, sub-
885 sampling and characterization of cryptomelane grains before the isotopic dating.
886

887 **Figure 5**. Reflected-light photomicrographs of polished thin sections from samples
888 collected in Sandur **(a-b)** Shimoga **(c-d)** and Goa pits **(e-f-g)**, showing cryptomelane
889 (C), pyrolusite (P), the protore matrix (Pr), iron oxides (Fe), lithiophorite (L) and pores
890 (V). h) SEM image showing gibbsite crystals over cryptomelane needles. See the table 1
891 for samples description.
892

893 **Figure 6.** Procedure to separate cryptomelane grain aliquots from two sample slabs **(a-**
894 **b)** of the Sandur profile using from left to right the thin section, μ-XRF mapping
895 (yellow rectangle on section) and reflected-light photomicrography (pink rectangle on
896 section). The μ-XRF map yields the composite colored image with Mn in blue, Fe in
897 red and K in green. C = Cryptomelane; P = Pyrolusite; G = Goethite; H = Hematite. See
898 the table 1 for samples description
899

900 **Figure 7.** Electron probe microanalyses of cryptomelane on polished thin sections. The
901 three poles of the ternary diagram are initially Mn, 10 K and 10 Al. The black, grey and

white diamonds are samples from Sandur, Shimoga and Goa, respectively. See also the data repository table DR1.

Figure 8. $^{40}Ar/^{39}Ar$ age spectra of cryptomelane grains showing regular ages, with K/Ca (black) and Ar* (grey) step curves (left), and inverse isochron diagrams (right). **(a)** Plateau age for Sandur's cryptomelane grain; **(b)** plateau age for Shimoga's cryptomelane grain with small characteristic $^{40}Ar^*$ losses from less retentive and poorly crystalline sites at the first step heating; **(c)** Forced-plateau age for Shimoga's sample grain including four apparent ages forming a reasonably flat segment; **(d)** Concordant pseudoplateaus ages for Sandur's cryptomelane grain included in the 2σ interval. MSWD = mean square weighted deviation of the inverse isochron. See the table 1 for sample description and the data repository DR2 and DR3.

Figure 9. Disturbed $^{40}Ar/^{39}Ar$ age spectra of cryptomelane grains from Shimoga Mn ore deposits with K/Ca (black) and Ar* (grey) step curves (left), and inverse isochron diagrams (right). **(a)** Hump shape spectrum that only allows estimation of maximum and minimum ages of the mixed youngest and oldest phases, respectively. **(b)** Saddle shape spectrum resulting from mixing between several phases (supergene or hypogene) that lead to incorporation of excess $^{40}Ar^*$. **(c)** Case with an inherited hypogene contaminant. In the first steps, only the supergene phase (~ 18 Ma) releases gas, the inverse isochron diagram clearly showing the contamination with a hypogene phase enriched in $^{40}Ar^*$. See the table 1 for sample description and the data repository tables DR2 and DR3.

926 **Figure 10**. $^{40}Ar/^{39}Ar$ age spectra of cryptomelane grains from Sandur Mn ore samples.
927 Sample ID with (F) when analyzed using a double vacuum Staudacher-type furnace
928 coupled with VG3600 mass spectrometer. Age quality is noted (A) for best quality first
929 order age, (B) for acceptable quality second order age, and (C) for lesser quality third
930 order age. See the table 1 for sample description, and the data repository table DR2.
931
932 **Figure 11**. **(a)** $^{40}Ar/^{39}Ar$ age spectra and **(b)** inverse isochron diagrams for
933 cryptomelane grains from Shimoga Mn ore samples. See the figure 10 for the analytical
934 system used, age quality explanation and the table 1 for sample description. See also the
935 data repository tables DR2 and DR3.
936
937 **Figure 12**. **(a)** $^{40}Ar/^{39}Ar$ age spectra and **(b)** inverse isochron diagrams for
938 cryptomelane grains from Goa Mn ore samples. See the figure 10 for the analytical
939 system used, age quality explanation and the table 1 for sample description. See also the
940 data repository tables DR2 and DR3.
941
942 **Figure 13**. Synthesis of the $^{40}Ar/^{39}Ar$ ages results accounting for two-confidence order
943 (A) and (B) (see text and figure 9 for explanations). **(a)** Age probability curves
944 accounting for 1/3 of the total signal from all the validated ages weighted for the three
945 distinct areas (N_{Sandur}=19, $N_{Shimoga}$=10 and N_{Goa}=10) enhancing the major weathering
946 peaks that document the major weathering periods W1, W2a, and W2b (vertical colored
947 bands). The ages are also plotted against the altitude. **(b)** Paleo-latitudinal variation of
948 the southern boundary of the Deccan Traps across climatic zones defined by
949 evaporation (E) and precipitation (P) after Kent and Muttoni (2008). Note the main

weathering periods derived from the $^{40}Ar/^{39}Ar$ ages in (a) also correspond to the period when peninsular India drift across the humid equatorial belt where P > E. **(c)** Global benthic $\delta^{18}O$ curve from Zachos et al. (2008) and associated global deep ocean temperature relative to actual T°C. PETM = Paleocene-Eocene Thermal Maximum; EECO = Early Eocene Climatic Optimum; MECM = Mid-Eocene Climatic Maximum; EOC = Early Oligocene Cooling; LOW = Late Oligocene Warming; MMCM = Mid-Miocene Climatic Maximum.

Table 1. Field characteristics of samples from Sandur, Shimoga and Goa Mn ore deposits (Peninsular India) and description of cryptomelane grains extracted from these samples. Other mineral species were also identified by reflected-light microscopy, XRD and SEM.

Table 2. Synthesis of the $^{40}Ar/^{39}Ar$ ages presenting the plateau ages, the inverse isochrons ages with their properties, and the integrated ages. The results in bold are considered as the preferred ages. See the figure 10 for more information about the analytical system used.

Figure 1
Click here to download high resolution image

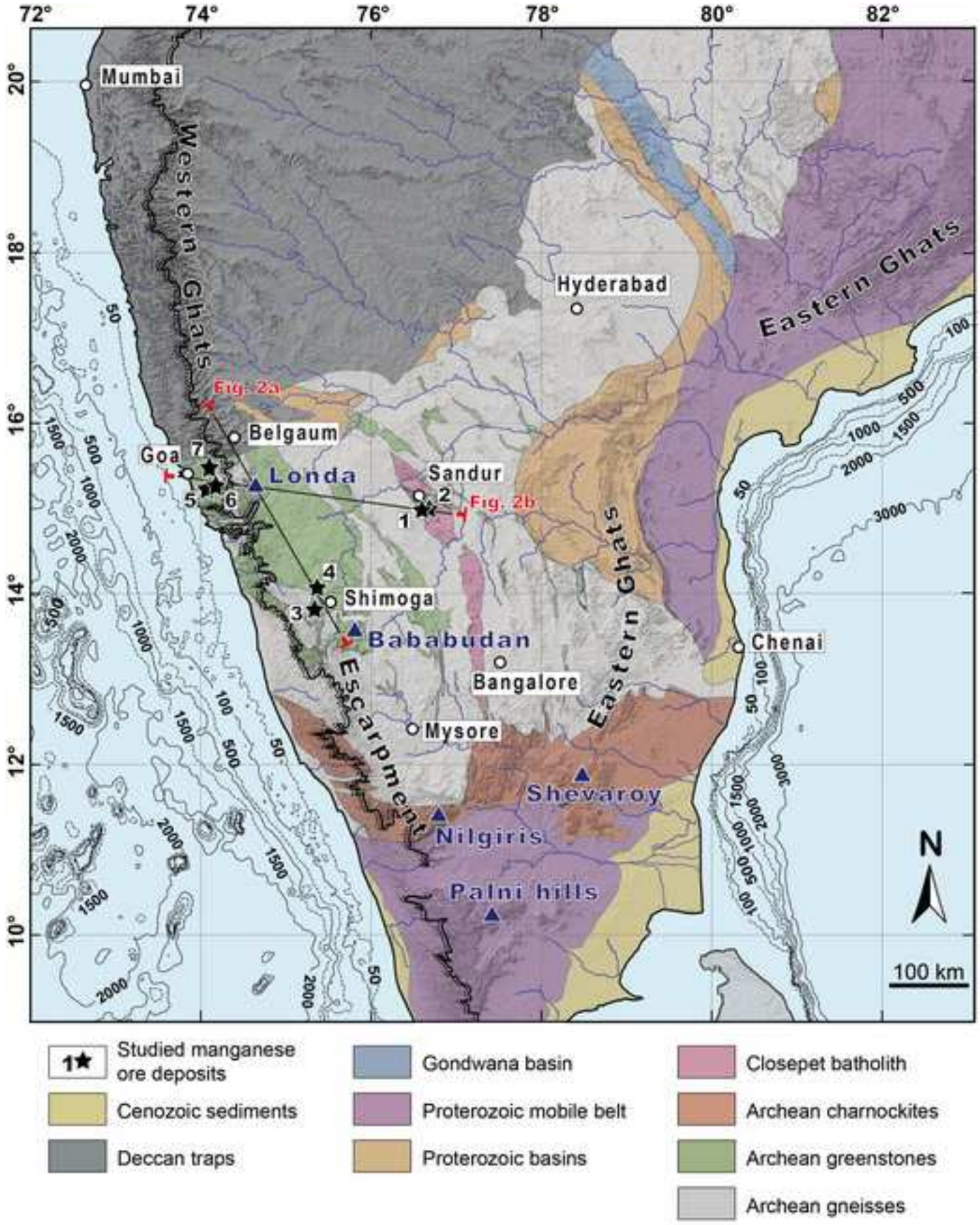

FIG. 1 (2 columns)

Figure 2

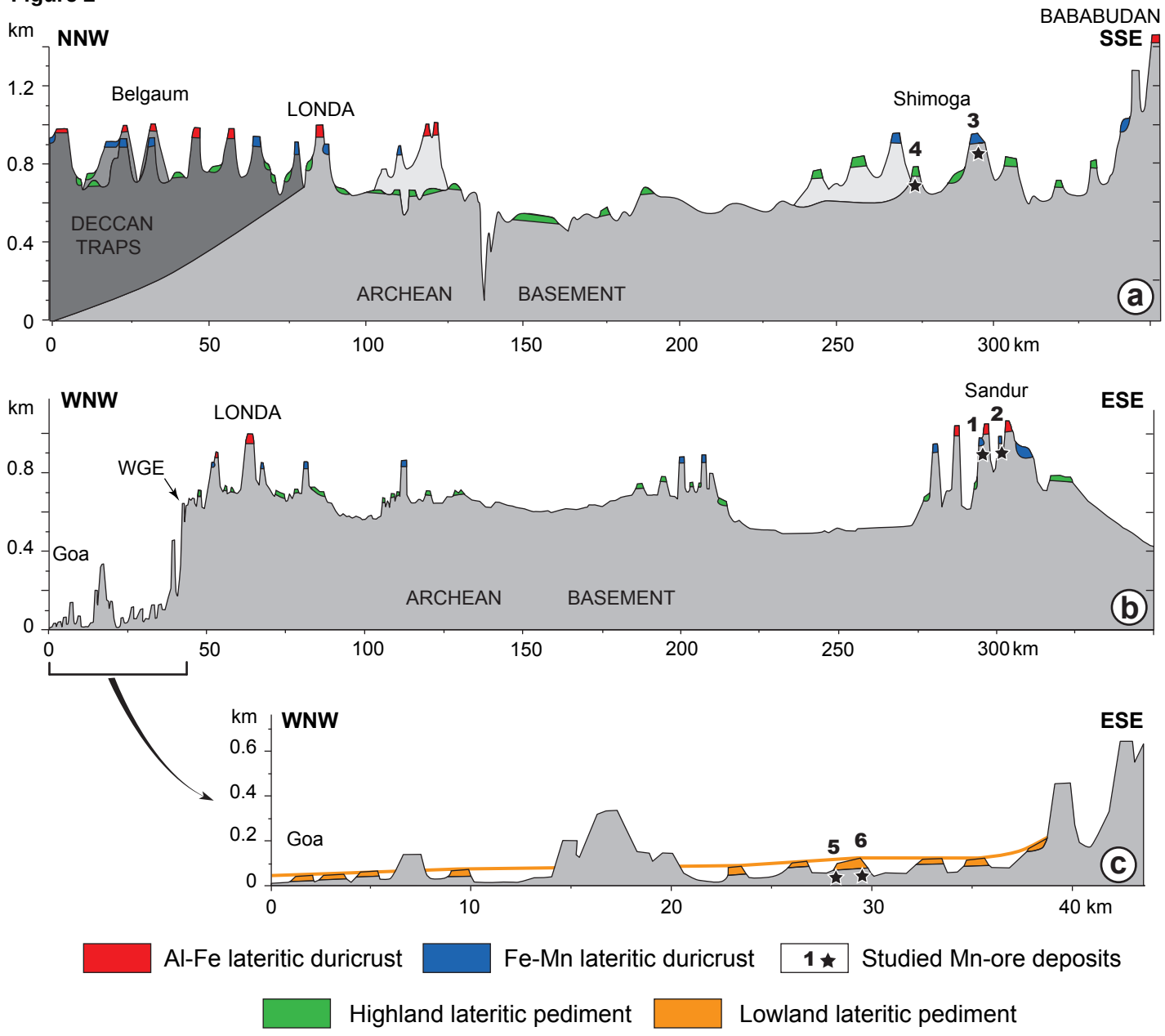

FIG.2 (2 columns)

Figure 3

Click here to download high resolution image

FIG. 3 (2 columns)

Figure 4

Click here to download high resolution image

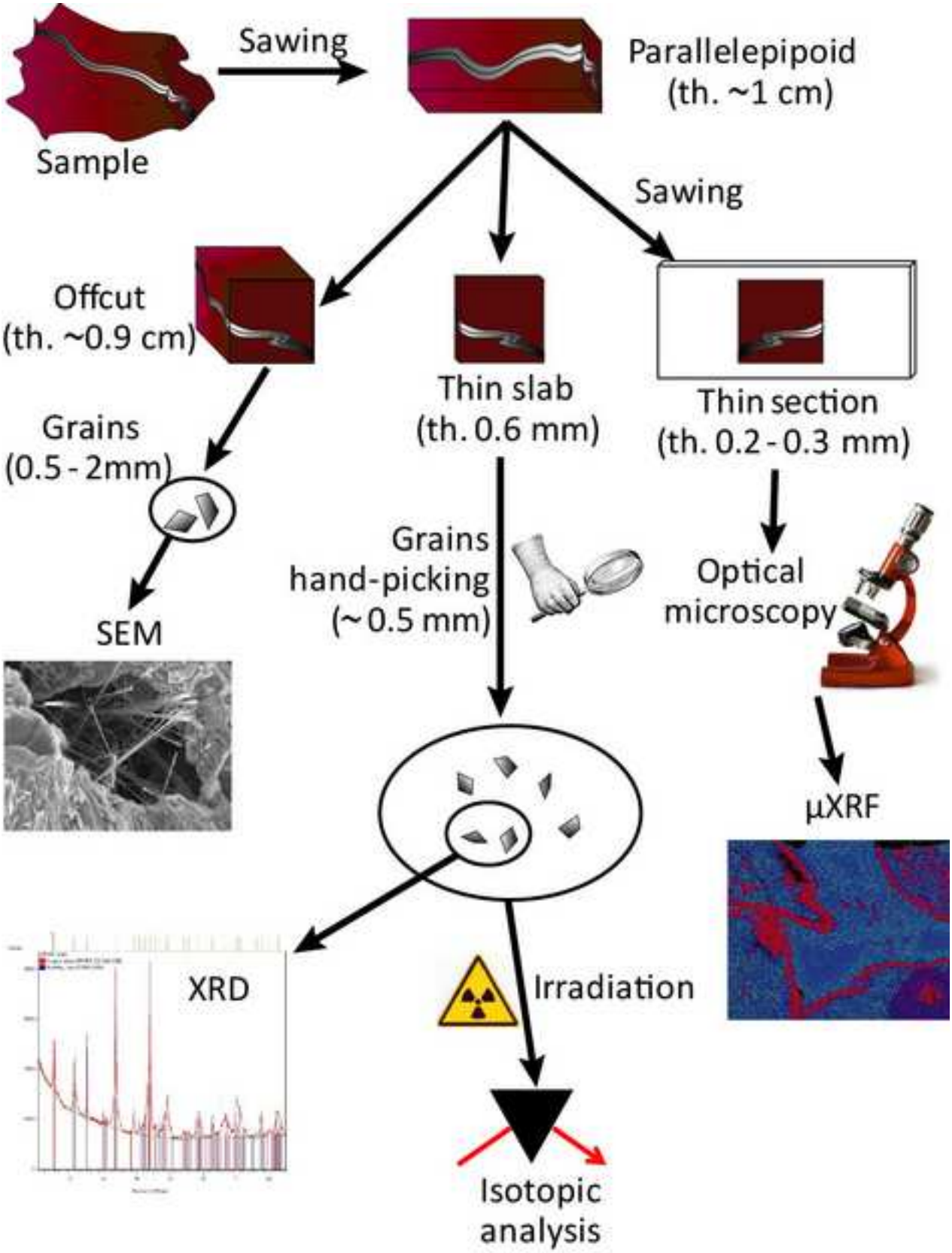

FIG. 4 (1 column)

Figure 5

Click here to download high resolution image

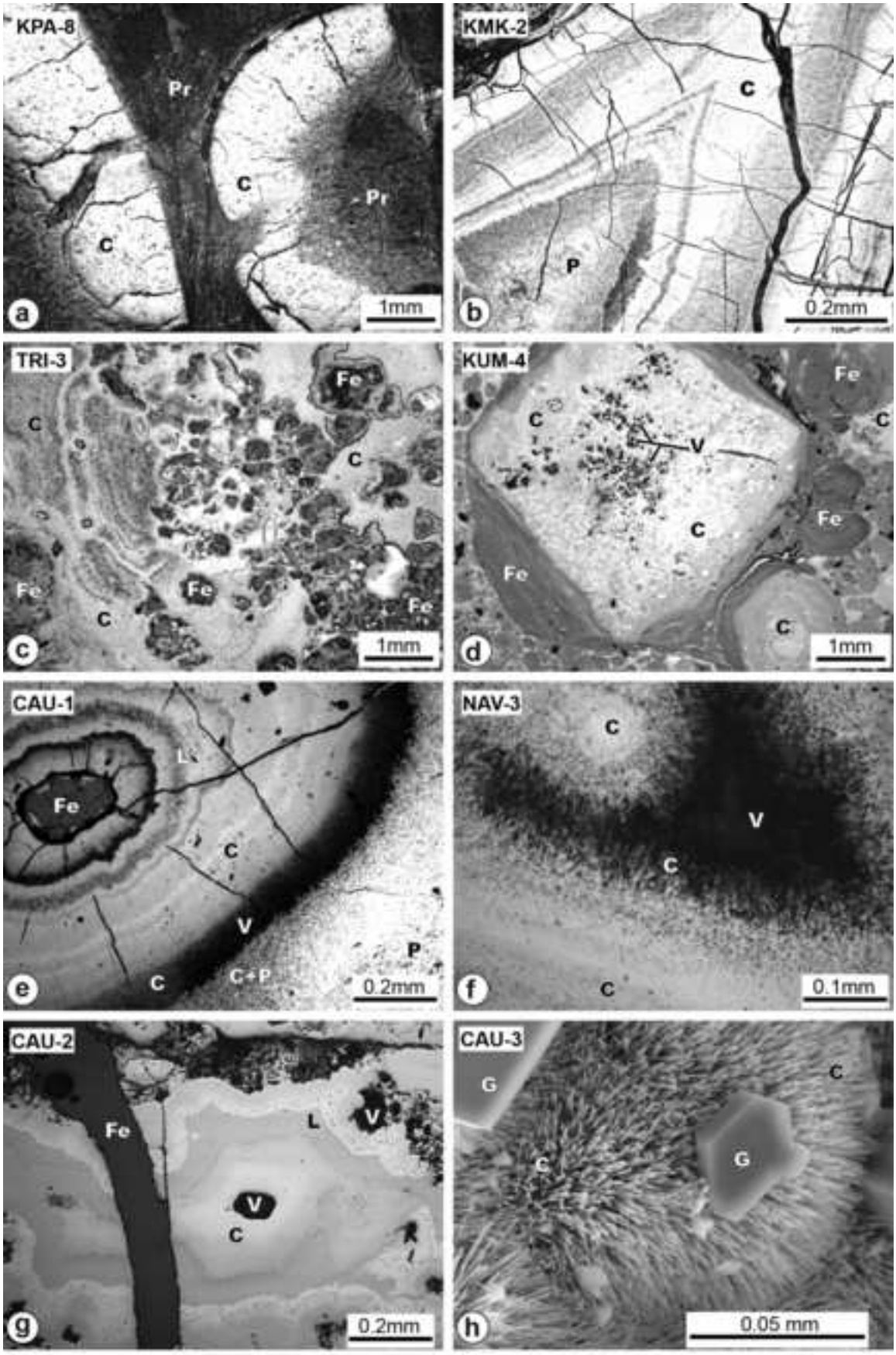

FIG. 5 (1.5 columns)

Figure 6

Click here to download high resolution image

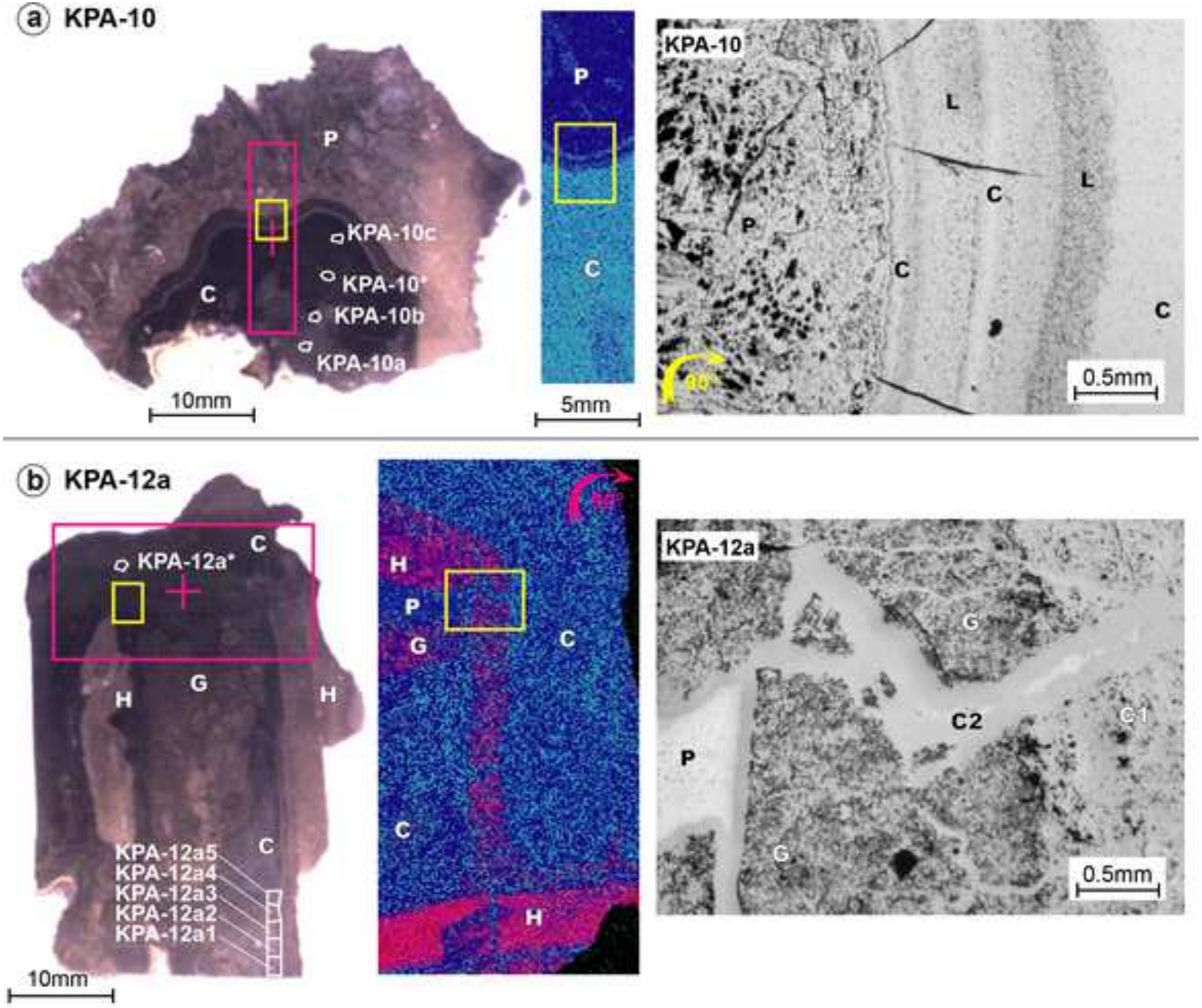

FIG. 6 (2 columns)

Figure 7
Click here to download high resolution image

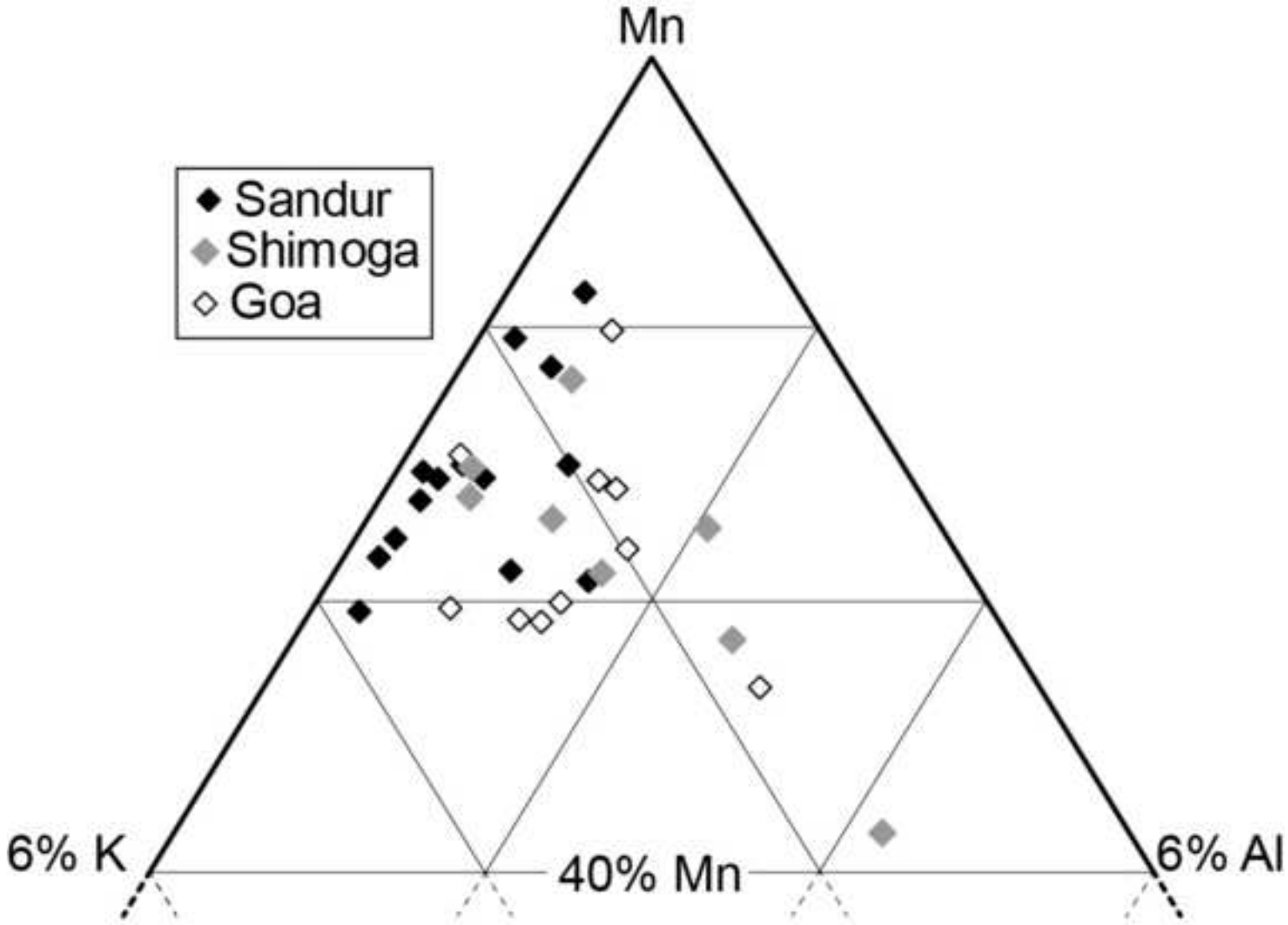

FIG. 7 (1 column)

Figure 8

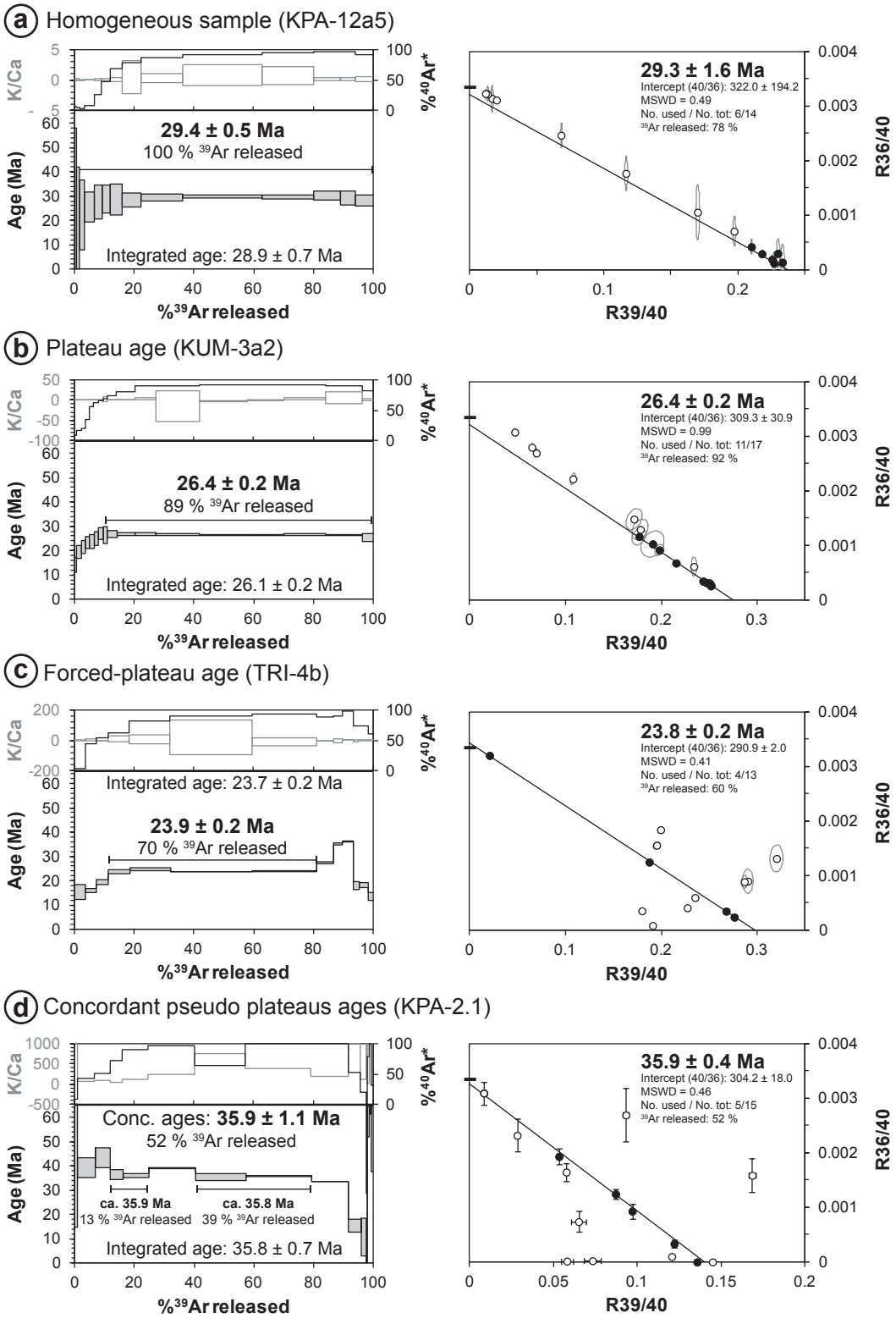

FIG. 8 (1.5 columns)

Figure 9

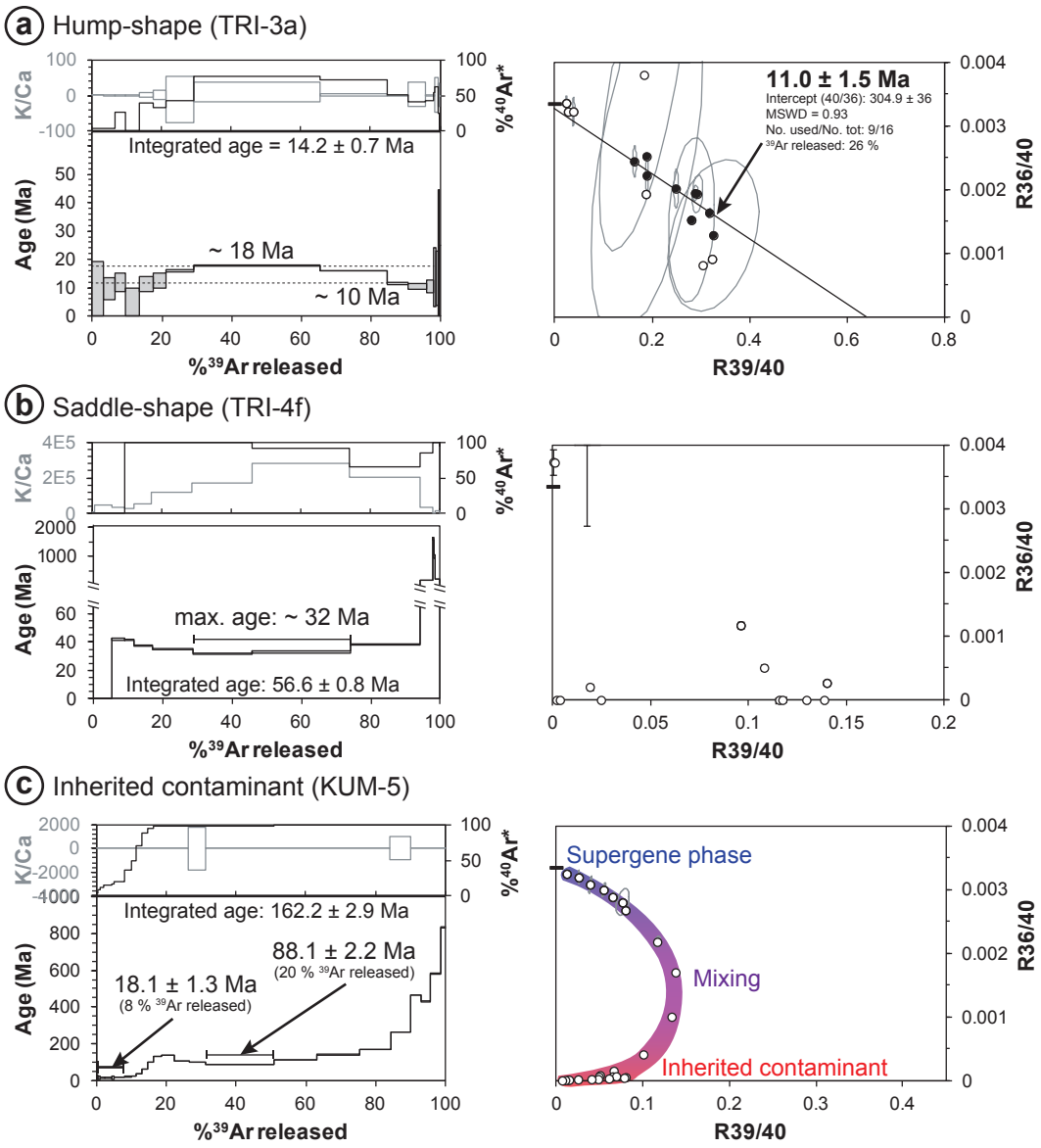

FIG. 9 (1.5 columns)

Figure 10

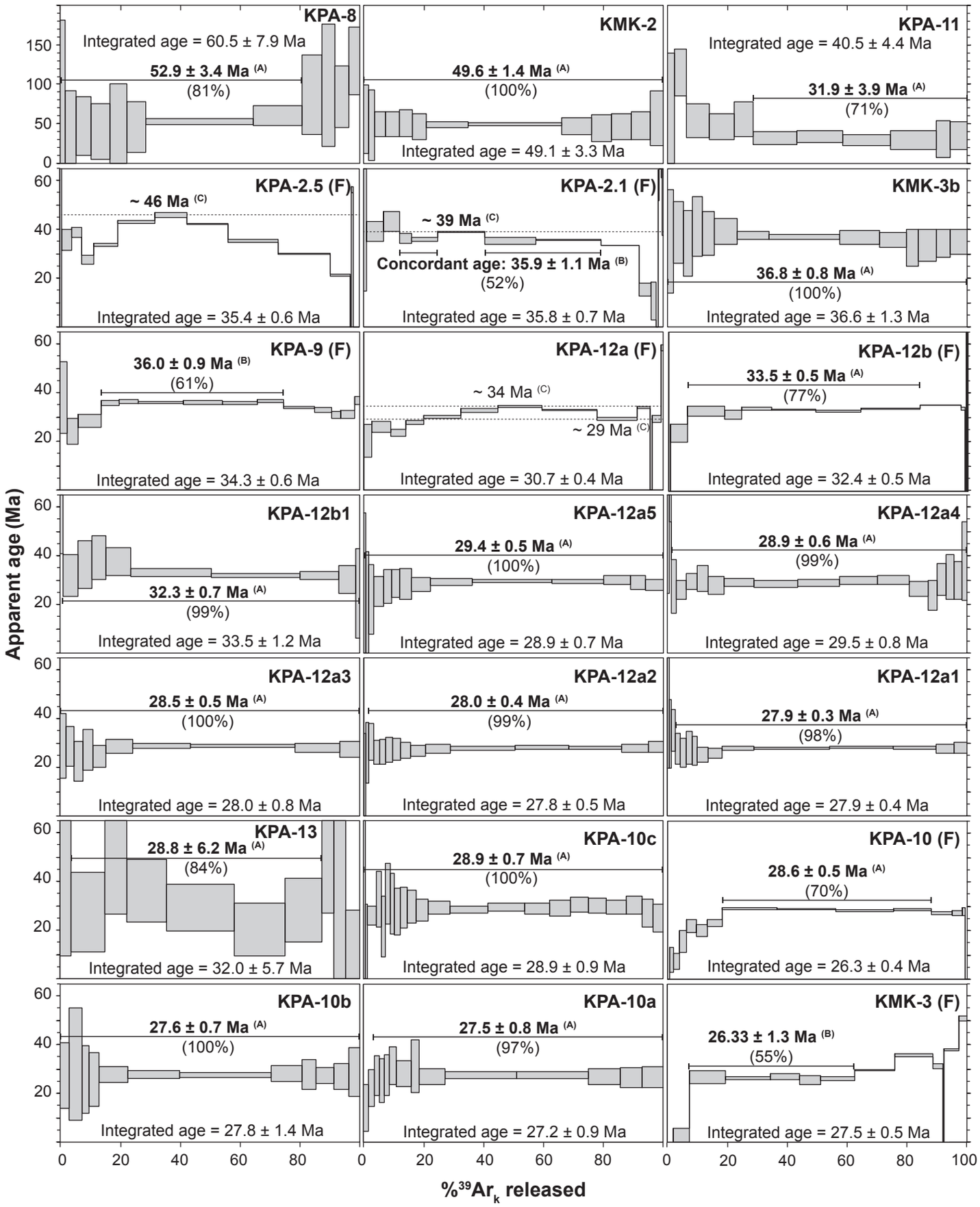

FIG. 10 (2 columns)

Figure 11

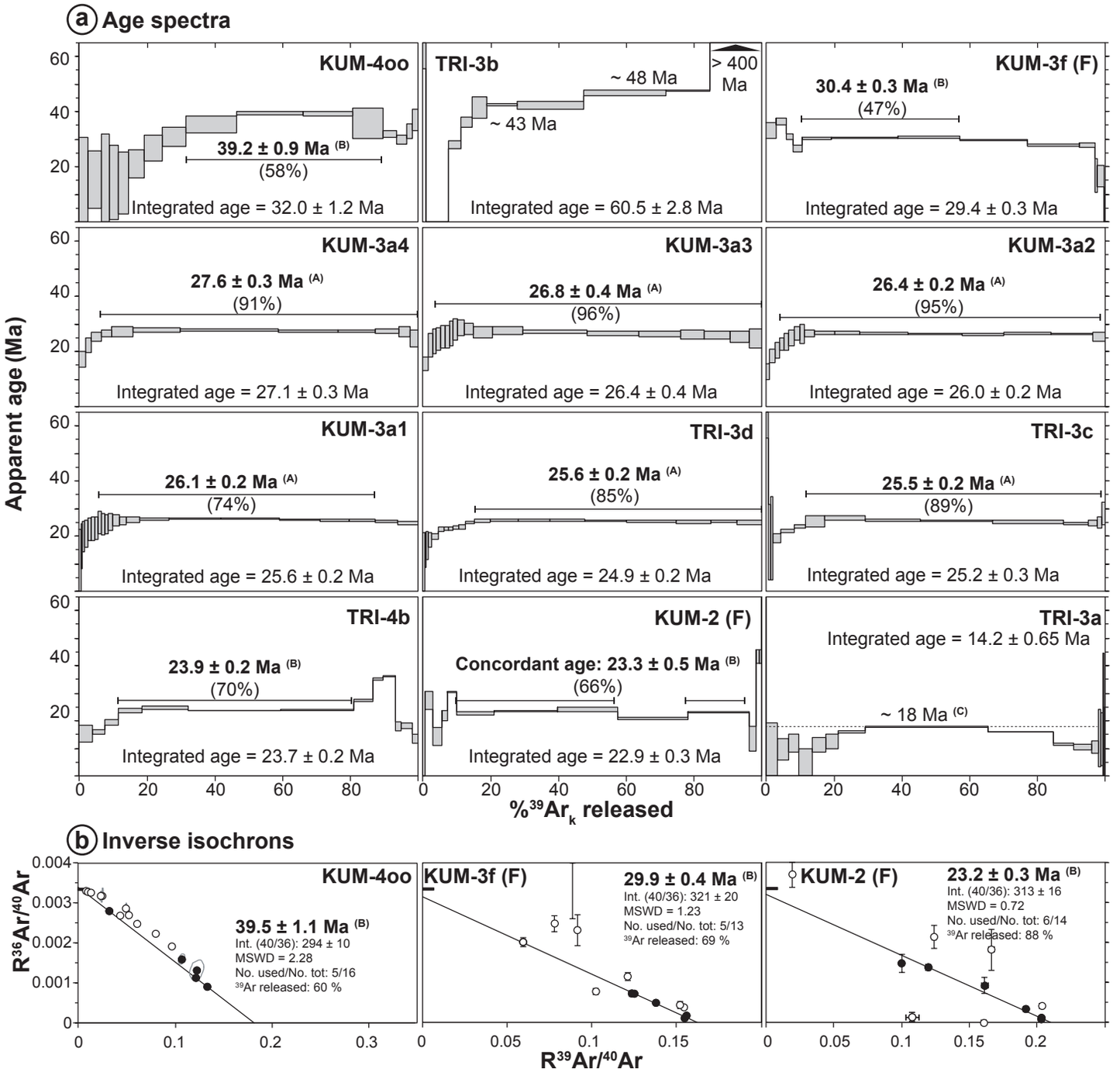

FIG. 11 (2 columns)

Figure 12

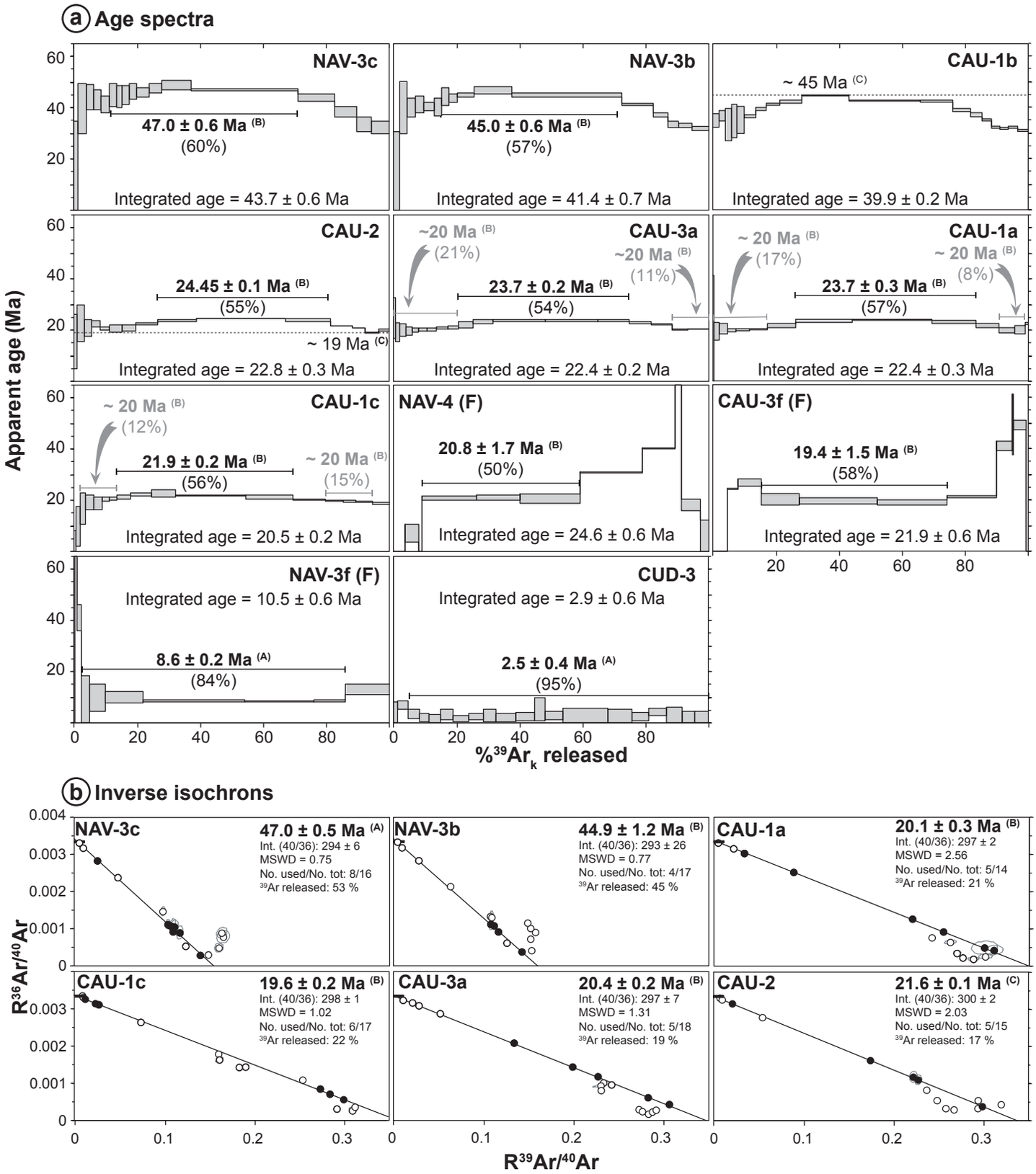

FIG. 12 (2 columns)

Figure 13

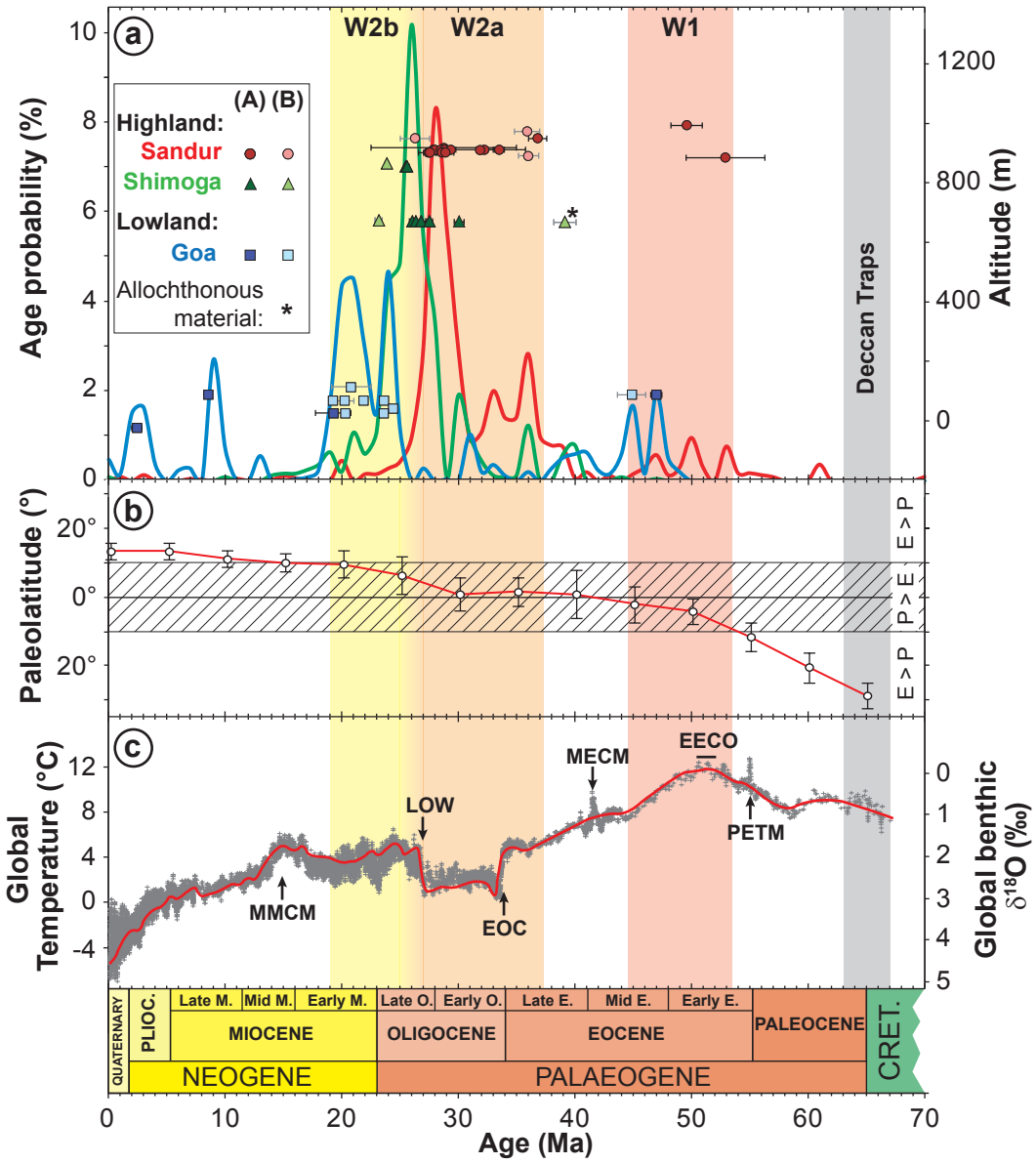

FIG. 13 (1.5 columns)

Table 1

Click here to download Table: R2_Table. 1.xlsx

Location and mine	Sample ID	Depth ± 2m	Latitude N	Longitude E	Ore type	Mineral species observed	Grains ID	Cryptomelane crystallization type
Sandur								
Kappataswamy								
	KPA-2	-140	14° 59' 59''	76° 32' 42''	Massive Mn-ore with cavities ≤ 1cm	Cryptomelane, Goethite, Nsutite, Pyrolusite	KPA-2.1 KPA-2.5	Internal band from colloidal overgrowth microstructure External band from colloidal overgrowth microstructure
	KPA-8	-125	15° 0' 2''	76° 32' 42''	Platy Mn-ore developed from siliceous protore	Cryptomelane, Pyrolusite, Lithiophorite	KPA-8	Botryoidal
	KPA-9	-123	15° 0' 1''	76° 32' 38''	Platy Mn-ore developed from siliceous protore	Cryptomelane, Quartz, Pyrolusite,	KPA-9	Massive cryptocrystalline domain
	KPA-10	-111	15° 0' 1''	76° 32' 38''	Massive Mn-ore with cavities > 1cm	Cryptomelane, Pyrolusite, Goethite, Hematite	KPA-10a KPA-10b KPA-10 KPA-10c	Internal band from geodic overgrowth microstructure 1st intermediate band from geodic overgrowth microstructure 2nd intermediate band from geodic overgrowth microstructure External band from geodic overgrowth microstructure
	KPA-11	-103	15° 0' 1''	76° 32' 38''	Platy Mn-ore developed from siliceous protore	Cryptomelane, Pyrolusite, Goethite,	KPA-11	Cryptocrystalline plasma filling a microfracture
	KPA-12a	-102	15° 0' 1''	76° 32' 38''	Platy Mn-ore with pods	Cryptomelane, Goethite, Hematite	KPA-12a KPA-12a1 KPA-12a2 KPA-12a3 KPA-12a4 KPA-12a5	Cryptocrystalline domain filling a microfracture Massive cryptocrystalline domain Massive cryptocrystalline domain Massive cryptocrystalline domain Massive cryptocrystalline domain Massive cryptocrystalline domain
	KPA-12b	-102	15° 0' 1''	76° 32' 38''	Platy Mn-ore with pods	Cryptomelane, Pyrolusite	KPA-12b KPA-12b2	Massive cryptocrystalline domain Massive cryptocrystalline domain
	KPA-13	-96	15° 0' 1''	76° 32' 37''	Platy Mn-ore developed from siliceous protore	Cryptomelane, Birnessite, Hematite	KPA-13	Veins of cryptocrystalline plasma
Channanghi KMK-East								
	KMK-2	-37	14° 59' 48''	76° 34' 37''	Massive Mn-ore with cavities > 1cm	Cryptomelane, Pyrolusite, Lithiophorite	KMK-2	Colloidal overgrowth microstructure
	KMK-3	-60	14° 59' 46''	76° 34' 38''	Massive Mn-ore with cavities > 1cm	Cryptomelane, Nsutite, Lithiophorite	KMK-3 KMK-3b	External band from colloidal overgrowth microstructure Internal band from colloidal overgrowth microstructure
Shimoga								
Triveni								
	TRI-3	-18	13° 53' 50''	75° 24' 46''	Massive developed from Banded Hematite Quartzite	Cryptomelane, Goethite, Birnessite	TRI-3a TRI-3b TRI-3c TRI-3d	Massive cryptocrystalline domain Massive cryptocrystalline domain Massive cryptocrystalline domain Massive cryptocrystalline domain
	TRI-4	-8	13° 53' 46''	75° 24' 43''	Massive developed from Banded Hematite Quartzite	Cryptomelane, Pyrolusite, Lithiophorite	TRI-4b TRI-4f	Massive cryptocrystalline domain Massive cryptocrystalline domain
Kumsi								
	KUM-2	-15	14° 6' 11''	75° 24' 15''	Massive developed from Banded Hematite Quartzite	Cryptomelane, Goethite, hematite	KUM-2	Massive cryptocrystalline domain
	KUM-3	-18	14° 6' 11''	75° 24' 14''	Massive developed from Banded Hematite Quartzite	Cryptomelane, Pyrolusite, Hematite	KUM-3a1 KUM-3a2 KUM-3a3 KUM-3a4 KUM-3f	Massive cryptocrystalline domain Massive cryptocrystalline domain Massive cryptocrystalline domain Massive cryptocrystalline domain Massive cryptocrystalline domain
	KUM-4	-20	14° 6' 10''	75° 24' 15''	Brecchia with manganiferous clasts and ferruginous oolithes	Cryptomelane, Hollandite, Hematite	KUM-4oo	Clast initially from massive cryptocrystalline domain
	KUM-5	-21	14° 6' 11''	75° 23' 55''	Massive developed from Banded Hematite Quartzite	Cryptomelane, Lithiophorite, Goethite, Kaolinite	KUM-5	Veins of cryptocrystalline plasma
Goa								
Caurem								
	CAU-1	-32	15° 7' 2''	74° 8' 40''	Clastic with ferruginous and manganiferous clasts	Cryptomelane, Pyrolusite, Goethite, Lithiophorite, Hematite	CAU-1a CAU-1b CAU-1c	Colloidal overgrowth microstructure Colloidal overgrowth microstructure Colloidal overgrowth microstructure
	CAU-2	-39	15° 7' 3''	74° 8' 40''	Fe-oxides with Mn-rich veins filled by percolation	Cryptomelane, Hematite, Lithiophorite, Kaolinite	CAU-2	Porous domains with visible needles
	CAU-3	-55	15° 7' 3''	74° 8' 39''	Clastic with ferruginous and manganiferous clasts	Cryptomelane, Hollandite, Goethite, Gibbsite	CAU-3a CAU-3f	Internal band from colloidal overgrowth microstructure External band from colloidal overgrowth microstructure
Naveli								
	NAV-3	-56	15° 7' 55''	74° 9' 50''	Manganiferous lens included in saprolite	Cryptomelane, Nsutite	NAV-3b NAV-3c NAV-3f	Massive cryptocrystalline domain Massive cryptocrystalline domain Cryptocrystalline plasma filling a microfracture
	NAV-4	-27	15° 8' 7''	74° 9' 32''	Accumulation of manganese in plurimetric lenses	Cryptomelane, Goethite	NAV4	Massive cryptocrystalline domain
Cudnem								
	CUD-3	-74	15° 32' 35''	74° 2' 3''	Brecchia with manganiferous clasts and ferruginous oolithes	Cryptomelane, Hollandite, Hematite	CUD-3	Massive cryptocrystalline domain

Sample			^{39}Ar release spectrum				Inverse isochron						Integrated Age, Ma	Preferred age		
Location	ID	Alt. (m)	Age, Ma	Step(s)	%^{39}Ar	Order	Age, Ma	40Ar/36Ar$_I$	MSWD	Steps	%^{39}Ar	Order		Ma	Order	Comments
SANDUR																
2	**KMK-2²**	996	**49,6 ± 1,4**	**1-13**	**100**	**A**	49,8 ± 2,8	285 ± 201	0,11	4-10	69	B	49,1 ± 3,3	**49,6 ± 1,3**	**A**	**Plateau > 70% $^{39}Ar_K$**
2	**KMK-3b**	952	**36,8 ± 0,8**	**1-15**	**100**	**A**	36,8 ± 1,2	425 ± 643	0,62	3, 6-11	72	B	36,6 ± 1,3	**36,8 ± 0,8**	**A**	**Plateau > 70% $^{39}Ar_K$**
2	**KMK-3 (F)¹**	952	**26,3 ± 1,3**	**3-7**	**55**	**B**	25,9 ± 0,8	305 ± 29	0,17	3-7	55	B	27,5 ± 0,5	**26,3 ± 1,3**	**B**	**Plateau > 50% $^{39}Ar_K$**
1	**KPA-13**	919	**28,8 ± 6,2**	**2-7**	**84**	**A**	27,6 ± 6,7	314 ± 293	1,19	2, 4-7	77	B	32,0 ± 5,7	**28,8 ± 6,2**	**A**	**Plateau > 70% $^{39}Ar_K$**
1	**KPA-12b (F)¹**	913	**33,5 ± 0,5**	**3-8**	**77**	**A**	33,6 ± 0,4	292 ± 4	0,94	3-8, 10	78	C	32,4 ± 0,5	**33,5 ± 0,5**	**A**	**Plateau > 70% $^{39}Ar_K$**
1	**KPA-12b1**	913	**32,3 ± 0,7**	**2-11**	**99**	**A**	32,1 ± 0,8	343 ± 64	1,12	3-10	94	A	33,5 ± 1,2	**32,3 ± 0,7**	**A**	**Plateau > 70% $^{39}Ar_K$**
1	**KPA-12a (F)¹**	913	34,3 ± 0,3 28,6 ± 0,9	8 5	14 6	C C	28,7 ± 0,6	336 ± 24	0,86	5-7, 10, 13	47	C	30,7 ± 0,4	34,3 ± 0,3 28,6 ± 0,9	C C	Min. of oldest Max. of youngest
1	**KPA-12a1**	913	**27,9 ± 0,3**	**4-15**	**98**	**A**	27,9 ± 0,3	297 ± 14	1,05	4-15	98	A	27,9 ± 0,4	**27,9 ± 0,3**	**A**	**Plateau > 70% $^{39}Ar_K$**
1	**KPA-12a2**	913	**28,0 ± 0,4**	**3-15**	**99**	**A**	28,1 ± 0,4	299 ± 8	0,70	3-6, 9, 11-13	70	A	27,8 ± 0,5	**28,0 ± 0,4**	**A**	**Plateau > 70% $^{39}Ar_K$**
1	**KPA-12a3**	913	**28,5 ± 0,5**	**1-10**	**100**	**A**	28,6 ± 0,5	292 ± 17	0,99	2-9	92	A	28,0 ± 0,8	**28,5 ± 0,5**	**A**	**Plateau > 70% $^{39}Ar_K$**
1	**KPA-12a4**	913	**28,9 ± 0,6**	**3-18**	**99**	**A**	28,9 ± 0,7	312 ± 57	1,02	5-18	94	A	29,5 ± 0,8	**28,9 ± 0,6**	**A**	**Plateau > 70% $^{39}Ar_K$**
1	**KPA-12a5**	913	**29,4 ± 0,5**	**1-14**	**100**	**A**	29,3 ± 1,6	322 ± 194	0,49	9-14	78	A	28,9 ± 0,7	**29,4 ± 0,5**	**A**	**Plateau > 70% $^{39}Ar_K$**
1	**KPA-11v**	912	**31,9 ± 3,9**	**6-11**	**71**	**A**	31,3 ± 5,3	380 ± 94	0,33	3, 5-9	75	B	40,5 ± 4,4	**31,9 ± 3,9**	**A**	**Plateau > 70% $^{39}Ar_K$**
1	**KPA-10a**	904	**27,5 ± 0,8**	**3-14**	**97**	**A**	27,6 ± 1,1	296 ± 855	0,43	4, 6-8, 10-11, 13	67	B	27,2 ± 0,9	**27,5 ± 0,8**	**A**	**Plateau > 70% $^{39}Ar_K$**
1	**KPA-10b**	904	**27,6 ± 0,7**	**1-12**	**100**	**A**	27,6 ± 0,8	299 ± 370	0,06	5-12	87	B	27,8 ± 1,4	**27,6 ± 0,5**	**A**	**Plateau > 70% $^{39}Ar_K$**
1	**KPA-10 (F)¹**	904	**28,6 ± 0,5**	**8-12**	**70**	**A**	28,8 ± 0,6	301 ± 38	0,83	8-9, 11, 13-14	54	A	26,3 ± 0,4	**28,6 ± 0,5**	**A**	**Plateau > 70% $^{39}Ar_K$**
1	**KPA-10c**	904	**28,9 ± 0,7**	**1-22**	**100**	**A**	28,9 ± 1,1	294 ± 262	0,96	5, 10, 13-14, 17, 19, 21-22	49	A	28,9 ± 0,9	**28,9 ± 0,7**	**A**	**Plateau > 70% $^{39}Ar_K$**
1	**KPA-9 (F)¹**	892	**36,0 ± 0,9**	**4-9**	**61**	**B**	36,2 ± 0,5	293 ± 23	0,37	4, 6, 8-9, 14	43	B	34,3 ± 0,6	**36,0 ± 0,9**	**B**	**Plateau > 50% $^{39}Ar_K$**
1	**KPA-8²**	887	**52,9 ± 3,4**	**1-8**	**81**	**A**	52,1 ± 4,9	339 ± 133	0,89	4-9	77	A	60,5 ± 7,9	**52,9 ± 3,4**	**A**	**Plateau > 70% $^{39}Ar_K$**
1	**KPA-2.5 (F)¹**	875	46,0 ± 1,1 21,2 ± 0,4	7 11	11 6	C NGS	35,1 ± 0,7	299 ± 12	2,29	1-3, 5, 9	32	NGS	35,4 ± 0,6	46,0 ± 1,1	C	Min. of oldest
1	**KPA-2.1 (F)¹**	875	35,9 ± 1,1 39,1 ± 0,3	4-5, 7-8 6	52 16	B C	**35,9 ± 0,4**	**304 ± 18**	**0,46**	**4-5, 7-8, 14**	**52**	**B**	35,8 ± 0,7	**35,9 ± 1,1**	**B**	**Best fitted inverse isochrone**
SHIMOGA																
3	**TRI-4b**	867	**23,9 ± 0,2**	**4-7**	**70**	**B**	23,8 ± 0,2	291 ± 2	0,41	1, 4, 6-7	60	C	23,7 ± 0,2	**23,9 ± 0,2**	**B**	**Forced-plateau**
3	**TRI-3a**	857	17,8 ± 0,2 10,4 ± 1,0	8 11-12	36 5	C C	11,0 ± 1,5	306 ± 36	0,93	3, 5-6, 10-15	26	C	14,2 ± 0,7	17,8 ± 0,2 10,4 ± 1,0	C C	Min. of oldest Max. of youngest
3	**TRI-3b**	857	42,6 ± 0,3	5-7	33	C	42,6 ± 2,0	297 ± 232	0,36	5-7	33	NGS	60,5 ± 2,8	42,6 ± 0,3	C	Max. age
3	**TRI-3c**	857	**25,5 ± 0,2**	**7-14**	**89**	**A**	25,5 ± 0,5	353 ± 100	1,01	7-10, 14	57	A	25,2 ± 0,3	**25,5 ± 0,2**	**A**	**Plateau > 70% $^{39}Ar_K$**
3	**TRI-3d**	857	**25,7 ± 0,2**	**12-20**	**87**	**A**	25,5 ± 0,4	281 ± 89	1,86	11-12, 15-20	70	B	24,9 ± 0,2	**25,7 ± 0,2**	**A**	**Plateau > 70% $^{39}Ar_K$**
4	**KUM-2 (F)**	675	23,3 ± 0,5	6-8, 10	66	B	**23,3 ± 0,3**	**307 ± 16**	**0,65**	**4, 6-8, 10**	**67**	**B**	22,9 ± 0,3	**23,2 ± 0,3**	**B**	**Best fitted inverse isochrone**
4	**KUM-3a1**	672	**26,1 ± 0,2**	**8-20**	**74**	**A**	25,2 ± 0,7	296 ± 17	0,92	6-14, 22	20	B	25,6 ± 0,2	**26,1 ± 0,2**	**A**	**Plateau > 70% $^{39}Ar_K$**
4	**KUM-3a2**	672	**26,4 ± 0,2**	**5-17**	**95**	**A**	26,4 ± 0,3	303 ± 28	1,02	7-16	93	A	26,0 ± 0,2	**26,4 ± 0,2**	**A**	**Plateau > 70% $^{39}Ar_K$**
4	**KUM-3a3**	672	**26,8 ± 0,4**	**4-19**	**96**	**A**	26,9 ± 0,5	294 ± 18	1,11	3-19	97	A	26,4 ± 0,4	**26,9 ± 0,4**	**A**	**Plateau > 70% $^{39}Ar_K$**
4	**KUM-3a4**	672	**27,6 ± 0,3**	**4-11**	**91**	**A**	27,7 ± 0,5	293 ± 36	0,94	5-9	78	A	27,1 ± 0,3	**27,6 ± 0,3**	**A**	**Plateau > 70% $^{39}Ar_K$**
4	**KUM-3f (F)**	672	30,4 ± 0,4	5-7	47	NGS	29,9 ± 0,4	321 ± 20	1,23	3, 5-8	69	NGS	29,4 ± 0,3	**None**		$^{40}Ar^*$ recoil
4	**KUM-4oo**	670	**39,2 ± 0,9** 24,0 ± 3,0	**9-12** 1-7	**58** 24	**B** C	40,1 ± 4,4 26,6 ± 5,3	284 ± 79 293 ± 6	1,56 1,37	10-12 4-7	43 16	B C	32,0 ± 1,2	**39,2 ± 0,9**	**B**	**Forced-plateau**
GOA																
6	**NAV-4 (F)²**	113	**20,8 ± 1,7**	**6-8**	**54**	**B**	20,7 ± 0,9	296 ± 25	0,41	4, 6-8, 13	56	B	24,6 ± 0,6	**20,8 ± 1,7**	**B**	**Plateau > 50% $^{39}Ar_K$**
6	**NAV-3b²**	88	**45,0 ± 0,7**	**7-11**	**57**	**B**	44,9 ± 1,2	293 ± 26	0,77	7-9, 11	45	B	41,4 ± 0,7	**44,9 ± 1,2**	**B**	**Plateau > 50% $^{39}Ar_K$**
6	**NAV-3c²**	88	47,0 ± 0,6	6-13	60	B	**47,0 ± 0,5**	**294 ± 6**	**0,75**	**3, 6-11, 13**	**53**	**A**	43,7 ± 0,6	**47,0 ± 0,5**	**A**	**Best fitted inverse isochrone**
6	**NAV-3f (F)²**	88	**8,6 ± 0,2**	**4-9**	**84**	**A**	8,6 ± 0,6	309 ± 94	0,55	4-9	84	B	10,5 ± 0,6	**8,6 ± 0,2**	**A**	**Plateau > 70% $^{39}Ar_K$**
5	**CAU-1a²**	68	**23,7 ± 0,3** **20,1 ± 0,2**	**8-10** **1-6, 12-13**	**57** **26**	**B** **B**	23,7 ± 0,3 20,3 ± 0,8	293 ± 3 293 ± 25	1,99 0,45	3, 8-10 5-6, 12	59 15	C B	22,4 ± 0,3	**23,7 ± 0,3** **20,3 ± 0,8**	**B** **B**	**Plateau > 50% $^{39}Ar_K$** **Concordant pseudo-plateaus**
5	**CAU-1b**	68	44,7 ± 0,2 31,2 ± 0,4	10 19	15 15	C C	35,2 ± 0,8	294 ± 42	0,81	3-6, 15	13	NGS	39,9 ± 0,2	44,7 ± 0,2 31,2 ± 0,4	C C	Min. of oldest Max. of youngest
5	**CAU-1c²**	68	**21,9 ± 0,2** **19,7 ± 0,2**	**8-12** **3-7, 14-16**	**57** **27**	**B** **B**	22,0 ± 0,3 19,6 ± 0,2	299 ± 11 298 ± 1	1,77 1,02	8-11 3-5, 14-16	41 22	B B	20,5 ± 0,3	**21,9 ± 0,2** **19,3 ± 0,2**	**B** **B**	**Plateau > 50% $^{39}Ar_K$** **Concordant pseudo-plateaus**
5	**CAU-2**	41	**24,5 ± 0,1** 19,2 ± 0,2	**9-11** 13	**55** 4	**B** C	24,0 ± 0,2 21,6 ± 0,1	294 ± 3 297 ± 2	0,92 2,56	4, 9, 11 3, 5-7, 12	29 21	NGS C	22,8 ± 0,3	**24,5 ± 0,1** **20,2 ± 0,3**	**B** C	**Forced-plateau** Max. of youngest
5	**CAU-3a²**	25	**23,7 ± 0,2** **20,4 ± 0,2**	**10-14** **1-8, 17-18**	**54** **29**	**B** **B**	23,7 ± 0,2 20,4 ± 0,2	292 ± 2 297 ± 7	1,82 1,31	3-4, 11-14 5-7, 17-18	49 19	C B	22,4 ± 0,2	**23,7 ± 0,2** **20,4 ± 0,2**	**B** **B**	**Plateau > 50% $^{39}Ar_K$** **Concordant pseudo-plateaus**
5	**CAU-3f (F)²**	25	**19,4 ± 1,5**	**4-6**	**58**	**A**	20,2 ± 0,4	284 ± 18	0,05	4-6	58	C	21,9 ± 0,6	**19,4 ± 1,5**	**A**	**Plateau > 50% $^{39}Ar_K$**
7	**CUD-3**	-24	**2,5 ± 0,4**	**3-20**	**95**	**A**	2,1 ± 0,6	305 ± 11	0,18	3-20	95	B	2,9 ± 0,6	**2,5 ± 0,4**	**A**	**Plateau > 70% 39Ar$_K$**

(¹) recalculated after Bonnet et al., 2014; (²) recalculated after Beauvais et al, 2016
Locations: 1 = Kappataswamy pit; 2 = Channanghi KMK-East pit; 3 Triveni Pit; 4 = Kumsi pit; 5 = Caurem pit; 6 = Naveli pits; 7 Cudnem pit (See also Fig. 1)
Refer to Fig. 1 for localities numbers
A = 1st order age; B = 2nd order age; C = 3rd order age; NGS = No Geological Significance

TABLE 2

Data Repository 1 EPMA

Click here to download Background dataset for online publication only: Revised_DR1.xlsx

Data Repository 2 ArArCalc

Click here to download Background dataset for online publication only: R2_DR2.xlsx

Data Repository 3 Argon Integral

Click here to download Background dataset for online publication only: R2_DR3.xlsx

Data Repository Main Text

Click here to download Background dataset for online publication only: Revised_Data repositories-Main text_CHEMGE9048.doc